Biomedicine & Pharmacotherapy 199 (2026) 119371

Contents lists available at ScienceDirect

Biomedicine & Pharmacotherapy

journal homepage: www.elsevier.com/locate/biopha

Variant-dependent pharmacological rescue of phenylalanine hydroxylase supports a precision therapeutic strategy for phenylketonuria

María Conde-Giménez [a,b], Sandra Salillas [a,b], María Galiana-Cameo [a,b], Juan E. Martínez-Oliván [a,b], Alejandro Mahía [a,b], Manuel Ledesma [a,b], Juan José Galano-Frutos [a,b], Ritwik Maity [a,b], Adrián Velázquez-Campoy [a,b,c,d], María D. Díaz-de-Villegas [e], Ramón Hurtado-Guerrero [b,f,g], Javier Sancho [a,b,c,*]

[a] *Departamento de Bioquímica y Biología Molecular y Celular, Facultad de Ciencias, Universidad de Zaragoza, Zaragoza 50009, Spain*
[b] *Biocomputation and Complex Systems Physics Institute (BIFI)-GBsC-CSIC Joint Unit, Universidad de Zaragoza, Zaragoza 50018, Spain*
[c] *Aragon Health Research Institute (IIS Aragón), Zaragoza 50009, Spain*
[d] *CIBER de Enfermedades Hepáticas y Digestivas CIBERehd, Instituto de Salud Carlos III, Madrid 28029, Spain*
[e] *Instituto de Síntesis Química y Catálisis Homogénea (ISQCH)-Departamento de Química Orgánica, Facultad de Ciencias, Universidad de Zaragoza, Zaragoza 50009, Spain*
[f] *Copenhagen Center for Glycomics, Department of Cellular and Molecular Medicine, Faculty of Health Sciences, University of Copenhagen, Blegdamsvej 3, Copenhagen N, DK-2200, Denmark*
[g] *Fundación ARAID, Zaragoza 50018, Spain*

ARTICLE INFO

Keywords:
Phenylketonuria
Phenylalanine hydroxylase
Pharmacological chaperones
Drug repurposing
Belinostat
Tetrahydrobiopterin
Precision medicine
Rare metabolic disease

ABSTRACT

Phenylketonuria (PKU) is an inherited metabolic disorder caused by pathogenic variants in phenylalanine hydroxylase (PAH), leading to toxic phenylalanine accumulation and severe neurological complications if untreated. Current pharmacological treatment relies on tetrahydrobiopterin (BH4), which benefits only a subset of patients, highlighting a major unmet need for alternative therapies. Here, we combined high-throughput screening, computational modelling, and drug repurposing to identify pharmacological chaperones capable of rescuing PAH function. We evaluated 26 structurally diverse small molecules in HEK293T cells expressing wild-type PAH or one of eight PKU-associated variants spanning phenotypes from mild to classical disease. Chaperoning efficacy was strongly variant-dependent, and for every variant tested at least one compound produced a greater activity increase than BH4 under identical assay conditions. Notably, belinostat, a clinically approved histone deacetylase inhibitor, emerged as the most effective compound for several clinically severe variants. Mechanistically, functional rescue consistently correlated with an increased population of tetrameric, catalytically competent PAH, as quantified by mass photometry. The crystal structure of the PAH–belinostat complex (PDB ID: 9T1O), together with structural models for all compounds, provide a framework for rational optimization. These results establish a preclinical proof-of-concept for genotype-guided pharmacological chaperone therapy in PKU and support the feasibility of personalized, variant-specific treatment strategies.

1. Introduction

Disease labels often group together clinically similar conditions that arise from distinct underlying genotypes [1]. Such genetic heterogeneity can profoundly influence therapeutic efficacy, ultimately determining whether a treatment succeeds or fails [2–4]. Precision interventions tailored to patient-specific molecular features are therefore desirable in both polygenic and monogenic conditions [5]. Pharmacological chaperones (PCs) are conformation-selective small molecules that rescue destabilized proteins by binding specific folding or assembly states and shifting the corresponding equilibria toward functional, native-like conformations [6,7]. PCs have reached clinical translation, with approved compounds for several protein-misfolding disorders, including lysosomal storage diseases and channelopathies [8,9]. Conformation-selective ligands are particularly well suited to diseases in which pathogenic variants perturb protein folding or assembly in

---

* Correspondence to: Departamento de Bioquímica y Biología Molecular y Celular, Facultad de Ciencias, Universidad de Zaragoza, Zaragoza, 50009 Spain.
E-mail address: jsancho@unizar.es (J. Sancho).

https://doi.org/10.1016/j.biopha.2026.119371
Received 12 February 2026; Received in revised form 1 April 2026; Accepted 10 April 2026

distinct ways. Phenylketonuria (PKU) exemplifies this scenario. More than 2000 pathogenic variants have been identified in the gene encoding phenylalanine hydroxylase (PAH) (PAHvdb, http://www.biopku.org, accessed December 18, 2025), each potentially impairing enzyme function and therapeutic responsiveness to different extents. PKU is an autosomal recessive disorder that manifests when both PAH alleles carry deleterious variants and affects approximately 450,000 individuals worldwide [10]. Because PAH assembles as a tetramer, combinations of pathogenic monomers can theoretically give rise to more than 30 million distinct tetrameric assemblies—far exceeding the number of patients. This combinatorial diversity, together with the heterogeneous severity of individual variants, yields a wide spectrum of residual enzymatic activities linked to clinical phenotype, ranging from mild hyperphenylalaninemia to classical PKU [11]. At the severe end of this spectrum, reduced or absent PAH activity leads to elevated blood phenylalanine levels that, if untreated, cause progressive and irreversible neurological impairment [12]. Widespread neonatal screening has enabled early dietary intervention to limit phenylalanine intake in PKU. While effective in preventing neurological damage, this approach entails a strict and lifelong burden, underscoring the need for pharmacological alternatives. The most widely used pharmacological treatment for PKU is tetrahydrobiopterin (**BH_4**), the natural PAH cofactor, whose efficacy is strongly genotype-dependent. Oral **BH_4** administration can partially restore PAH activity and lower blood phenylalanine levels [13]. However, only ~40% of patients respond to **BH_4** [4,14], leaving the majority without benefit. Enzyme replacement therapy using recombinant human PAH could, in principle, treat all patients, but its clinical development has been precluded by the enzyme's intrinsic instability, proteolytic susceptibility, and potential immunogenicity [15]. A PEGylated bacterial phenylalanine ammonia lyase, capable of metabolizing phenylalanine, has been approved as an alternative approach, although its clinical use is limited by tolerability and immunogenicity concerns [15–17]. The therapeutic effect of **BH_4** has been attributed, at least in part, to its role as a pharmacological chaperone for destabilized PAH variants [18,19]. This observation has motivated the search for additional small molecules that could exert similar or greater chaperoning effects, particularly for the substantial fraction of patients who do not respond to **BH_4**.

Previously, we screened a chemically diverse library of 1000 compounds and identified several molecules that stabilized PAH and acted as PCs in vitro and in cell-based assays [20], with some also increasing PAH activity in mouse liver following oral administration. Guided by the X-ray structure of PAH bound to one of these compounds (**IV^{PC}**) [21], we designed and synthesized a second-generation series with enhanced affinity for human PAH [22]. In parallel, another group reported a different family of PCs identified through combined computational and experimental screening, with some compounds lowering blood phenylalanine levels in a mouse model [23]. Here, we report 10 newly discovered, structurally unrelated PCs and compare their activities with those of 14 previously described compounds, **BH_4**, and **belinostat**—a clinically approved drug with repurposing potential for PKU [24]. We evaluated the efficacy of all 26 compounds in HEK293T cells expressing wild-type PAH or one of eight pathogenic variants spanning the spectrum from mild to classical PKU. For each variant, multiple compounds outperformed **BH_4**. The identity of these compounds varied across variants, with only partial overlap among them. Together, these findings demonstrate that PAH pharmacochaperoning is strongly variant-dependent and establish a framework for genuinely personalized, "à la carte" therapies for PKU.

2. Results

2.1. Identification of structurally diverse PAH pharmacological chaperones by high-throughput screening

To expand the repertoire of pharmacological chaperones for PAH, we performed high-throughput screening (HTS) of two commercial libraries using differential scanning fluorimetry. The 10 compounds producing the largest thermal upshifts were selected and designated **PC1–10** (Table 1). All hits originated from the Maybridge Hit Finder Collection, exhibited no obvious structural similarity, and complied with Lipinski's guidelines [25]. Key physicochemical descriptors—including predicted lipophilicity, aqueous solubility, and drug likeness metrics—are summarized in Table S1. Some of these compounds appeared to display low solubility in the solutions used for crystallization trials (not shown). Predicted passive permeability and blood–brain barrier (BBB) penetration were assessed using the BOILED-Egg model [26] (Figure S1). Four compounds (**PC1**, **PC3**, **PC8**, **PC9**) showed suboptimal intestinal absorption, whereas **PC10** displayed a high likelihood of BBB penetration. Limiting BBB permeability is desirable in PKU, as the therapeutic effect—reduction of circulating phenylalanine—is achieved through restoration of hepatic PAH activity, making central exposure unnecessary. In contrast, brain penetration may introduce off-target effects, including interference with neurotransmitter biosynthesis and, for compounds with additional activities, potential central side effects. However, BBB permeability may be advantageous for targeting related aromatic amino acid hydroxylases, such as tyrosine or tryptophan hydroxylase, which may represent secondary targets for PAH-directed small molecules [27].

2.2. Thermostabilising effects and PAH affinities of PC1–10

PAH unfolds through a three-state equilibrium involving two thermal transitions—characterized by their transition temperatures, Tm1 and Tm2, the first of which primarily reflects unfolding of the catalytic domain [28]. For three-state unfolding equilibria, increases in Tm1 typically correlate with enhanced thermodynamic stability [29–31], making stabilization of this transition especially desirable. However, our previous work showed that **IV^{PC}** and its derivatives (compounds **IVx**) [22] predominantly stabilize the second transition, and that **IV^{PC}** rescues PAH activity through a combination of thermodynamic and kinetic mechanisms [20,21]. We evaluated the impact of **PC1–10** on PAH thermal unfolding and found that all ten compounds increased both transition temperatures (Fig. 1a). For **PC2**, **PC3**, **PC5**, and **PC7**, the two upshifts (ΔTm1 and ΔTm2) were comparable and ranged from 5.2 to 19.6 °C. In contrast, **PC1**, **PC4**, **PC6**, **PC8**, **PC9**, and **PC10** produced markedly larger upshifts in Tm2 (15–30 °C) than in Tm1 (5–8 °C) (Figure S2 and Table S2). Isothermal titration calorimetry revealed micromolar dissociation constants for all PAH–**PC1–10** complexes (Figure S3 and Table S3). Their thermodynamic signatures (Fig. 1b) closely resembled those of PAH–**IV^{PC}** and PAH–**IVx** complexes [22], with binding being predominantly entropy-driven and most compounds, except **PC4**, also displaying favourable enthalpic contributions.

2.3. Biophysical validation of belinostat (PC11) as a PAH thermostabilising ligand

Drug repurposing of clinically approved compounds may accelerate drug discovery by leveraging established safety and pharmacokinetic profiles. Using thermal proteome profiling [24] PAH was recently identified as a direct cellular target of panobinostat, an approved histone deacetylase inhibitor. Belinostat, a related approved histone deacetylase inhibitor that shares the N-hydroxycinnamide moiety with panobinostat, efficiently competes with panobinostat for PAH binding [24]. These findings prompted us to perform a biophysical analysis of **belinostat**–PAH interactions and to evaluate the chaperoning effects mediated by **belinostat** in cellular assays. Physicochemical and ADME properties of belinostat are summarized in Table S4. Belinostat exerts a clear thermostabilising effect on PAH thermal unfolding (ΔTm1 = 4.2 ± 0.4 °C and ΔTm2 = 4.0 ± 0.6 °C, Fig. 2a), forming a complex with micromolar affinity (Kd = 3.4 ± 0.6 μM). In contrast to complexes formed by previously analysed ligands, belinostat binding is characterized by

Table 1
New hit compounds identified by experimental screening as thermal stabilizers of human PAH[a].

Compound	Chemical structure	MW (g/mol)	CAS Registry Number
PC1	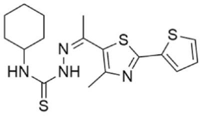	378.6	263147-98-4
PC2	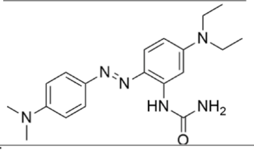	354.5	198010-51-4
PC3	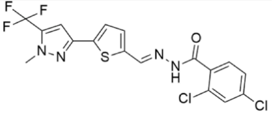	447.3	959571-32-5
PC4	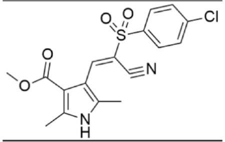	378.8	883002-04-8
PC5	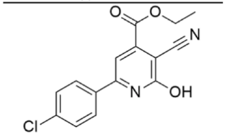	302.7	286430-73-7
PC6	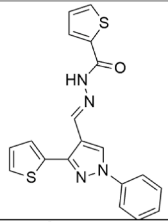	378.5	717097-67-1
PC7	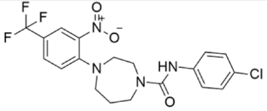	442.8	402563-20-6
PC8	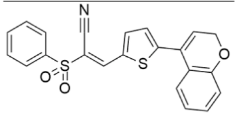	405.5	883030-72-6
PC9	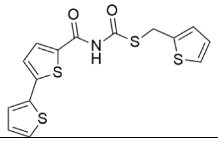	365.5	256327-42-1
PC10	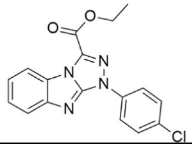	340.8	663193-56-4

[a] The chemical structures of PC12–13 and IVx derivatives are provided in Table S6 (Supplementary Material).

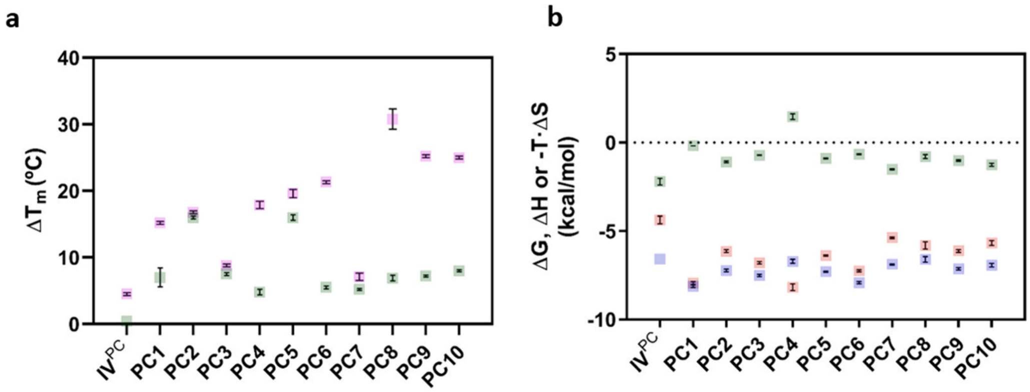

Fig. 1. Effect of compounds PC1–10 on PAH thermostability and thermodynamic binding profile of the PAH-PC1–10 complexes. (**a**) Comparative thermostabilising effect of **IV^{PC}** and **PC1–10** compounds at a 100 µM concentration, in presence of 2.5% DMSO. The thermal upshifts ΔT_{m1} (green) and ΔT_{m2} (pink) associated with each compound were calculated relative to the transition mid-temperatures of wild-type human PAH in the presence of 2.5% DMSO. Bars are propagated standard errors of the control and sample derived from the non-linear fits of the thermal unfolding curves. (b) Thermodynamic profiles of PAH-PC1–10 complexes. Binding Gibbs energy (ΔG) (violet), binding enthalpy (ΔH) (green), and entropic contribution to binding Gibbs energy ($-T \times \Delta S$) (red) were obtained from ITC experiments. Bars are standard errors (ΔG, ΔH) or propagated standard errors of the non-linear fits.

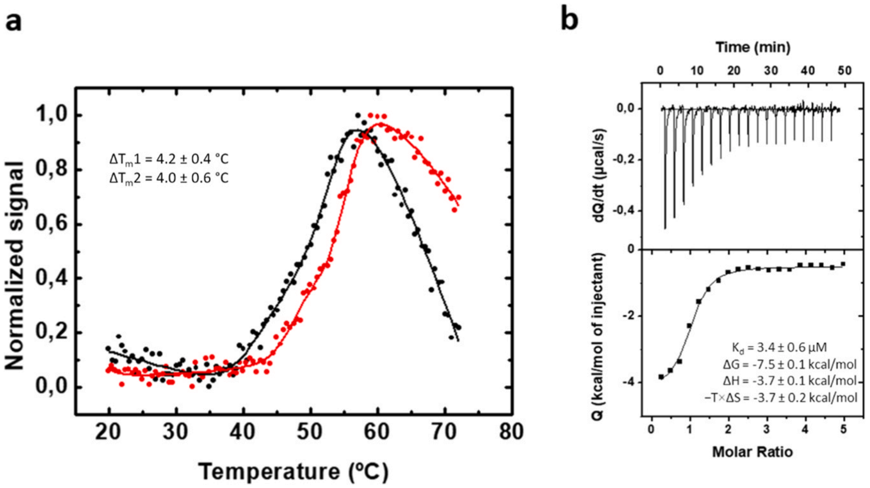

Fig. 2. Belinostat effect on recombinant PAH thermostability and thermodynamics of PAH-belinostat complex. (**a**) PAH thermal unfolding curves in the absence (black) or the presence of 100 µM **belinostat** (red). Continuous lines correspond to fits to a three-state unfolding model from where the indicated changes in T_m and associated errors are derived. In both experiments, the solution contained 2.5% DMSO. (**b**) Isothermal titration calorimetry of the PAH-**belinostat** complex. Upper panel: thermogram (thermal power required for maintaining the calorimetric cell at constant temperature, after baseline subtraction). Lower panel: binding isotherm (heat associated with each injection as a function of ligand-to-protein molar ratio). The thermodynamic data obtained for the complex from the non-linear fit of the binding isotherm are indicated. No correction was applied for proton exchange so the values correspond to those observed in PBS buffer at pH 7.4.

comparable enthalpic and entropic contributions (Fig. 2b).

2.4. X-ray structure of the PAH-belinostat complex

The X-ray structure of the PAH–**belinostat** complex (PDB ID 9T1O) was determined from crystals of the truncated dimeric form of human PAH obtained by soaking with belinostat. The crystals are orthorhombic and belong to the same space group ($C222_1$) previously reported for uncomplexed PAH [32] and for its complexes with **IV^{PC}** [21], 3,4-dihydroxyphenylalanine (L-DOPA) inhibitor [33], and the **BH$_4$** cofactor together with the 3-(2-thienyl)-alanine (THA) substrate analogue [34]. Unit cell dimensions and crystallographic statistics are provided in Table S5. The asymmetric unit contains one PAH monomer, which forms a dimer with a monomer located in a neighbouring asymmetric unit. Belinostat binds at the active site and participates, together with residues of the catalytic triad, in coordination of the catalytic iron atom (Fig. 3). The hydroxamate moiety of belinostat coordinates the iron asymmetrically through its two oxygen atoms, with Fe–O distances of 1.95 Å for the carbonyl oxygen and 2.69 Å for the hydroxyl oxygen. The active-site iron is coordinated by His285, His290 and Glu330, with Fe–Nε2 distances of 1.93 Å for His285 and 2.00 Å for His290, and an Fe–Oε1 distance of 2.18 Å for Glu330. The second oxygen atom of Glu330 lies at 2.80 Å and is therefore not considered a primary coordinating bond. Overall, the iron centre is best described as a distorted five-coordinate site with square-pyramidal character. This coordination closely matches that observed in the PAH–**IV^{PC}** complex [21] and differs from the six-coordinate octahedral geometry characteristic of unliganded PAH and its catecholamine complexes [32,33]. A similar five-coordinate metal centre has also been reported for tyrosine hydroxylase [35]. **Belinostat** further engages the protein through hydrogen bonds with Glu286 (distance of 2.5 Å), Ser251 (O–O distance of 3.3 Å and O-N distance of 2.7 Å), and a water molecule that also hydrogen-bonds to Glu286. The benzene ring of the N-hydroxycinnamide moiety forms a π-stacking interaction with Phe254. Nine ethylene glycol molecules from the crystallization and cryoprotectant solutions are present in the structure. Binding-site superposition (Figure S4) reveals a close overlap between the **belinostat** binding pose and those of other PAH ligands, including **IV^{PC}** [21], the L-DOPA

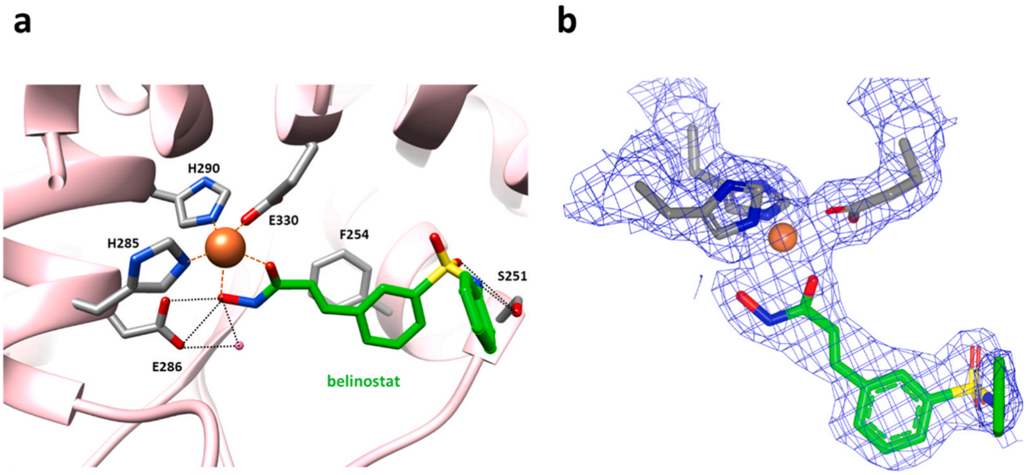

Fig. 3. Active site of the PAH-belinostat complex. (a) Binding of belinostat (green) at the active site of PAH. Belinostat acts as an asymmetrically bidentate ligand in the Fe^{3+} coordination sphere. The metal centre (brown sphere) is five-coordinate with the catalytic triad residues (light grey) and two oxygen atoms from belinostat. A water molecule (pink sphere) forms a hydrogen bond with belinostat; additional hydrogen bonds are shown as black dashed lines, and metal coordination to Fe^{3+} is shown as brown dashed lines. (b) Differential electron-density map (2Fo-Fc at 1σ, blue) of belinostat (green), the catalytic triad residues (grey), and the iron (pink sphere) are represented.

inhibitor [33] and the **BH$_4$** cofactor [34], consistent with **belinostat** acting as a competitive inhibitor. The overall structure of the PAH-**belinostat** complex closely resembles previously reported PAH structures (Figure S5). RMSD values relative to uncomplexed PAH (0.91 Å; Figure S5a), the IV^{PC} complex (0.48 Å; Figure S5b) and the L-DOPA complex (0.84 Å; Figure S5c) are all small. The largest RMSD (2.67 Å) is observed relative to the **BH$_4$**/THA ternary complex (Figure S5d), which was crystallized under anaerobic conditions and contains the metal centre in the ferrous state.

2.5. Docked models of PAH in complex with the evaluated compounds

Having established the binding mode of **belinostat** by X-ray crystallography, we next sought structural insight into PAH interactions with the remaining compounds. Attempts to obtain co-crystal structures of PAH with **PC1–PC10**, either by soaking pre-formed crystals or by co-crystallization, were unsuccessful. The high hydrophobicity and limited aqueous solubility of these PCs may have contributed to these difficulties [36–38]. We therefore employed a combined molecular docking and molecular dynamics (MD) strategy to generate structural models of PAH in complex with **PC1–10**, **PC12–13** and **IVx** derivatives (Table S6). To validate the docking protocol, **IV^{PC}**, **BH$_4$** and **belinostat** (PC11) were re-docked onto a previously generated full tetrameric PAH model (PAH-w; see Methods) under convergence conditions. For **IV^{PC}** and **BH$_4$**, good agreement with the crystallographic poses was obtained, with ligand RMSD (RMSD_lig) values of 1.0 Å and 1.6 Å, respectively, using the Vina scoring function (Fig. 4a,b). In contrast, the crystallographic binding mode of **belinostat** (Fig. 4c) was not accurately reproduced (RMSD_lig = 3.8 Å), likely because the PAH-w model includes the N-terminal domain, which is absent from the PAH–**belinostat** crystal structure reported here (PDB ID 9T1O) (Figure S6). This region is known to be conformationally flexible and to participate in regulatory movements that control access to the catalytic site [27].Under physiological conditions, such dynamics may influence the binding kinetics or affinity of belinostat. To alleviate steric clashes, N-terminal residues up to Gly33 were removed (Figure S6) and flexible-receptor docking was performed with side-chain flexibility allowed for Ser250, Ser251 and Tyr325. Under these conditions, the crystallographic pose of **belinostat** was accurately recovered (RMSD_lig = 1.9 Å, Fig. 4d) using the AD4 scoring function. Half-microsecond MD simulations were then carried out to assess the stability of the docked complexes. Only the system initialized from the flexible-docking pose of **belinostat** underwent clear local rearrangements, while maintaining bidentate coordination to the active-site Fe^{2+} ion (Fig. 4e,f), and the ligand frequently adopted conformations closely resembling the crystallographic pose (Fig. 4f).

Using this validated protocol, we next analysed the binding modes of the remaining compounds. The top-ranked binding poses and the corresponding Vina or AD4 binding energies are shown in Figure S7 for complexes of the PAH model with **PC1–PC10**, **PC12** and **PC13**, and in Figure S8 for complexes of the PAHw model with **IV^{PC}** derivatives. Nineteen of the 23 compounds analysed (**PC1–PC4**, **PC6**, **PC8**, **PC9**, **PC13**, **IVa**, **IVc–e**, **IVg**, **IVi**, and **IVm–q**) preferentially bound within the catalytic site. **PC5**, **PC7**, **PC10**, and **PC12** adopted binding poses located outside the active site, which did not coincide with previously proposed allosteric pockets [39,40]. For most ligands, binding appeared to be driven primarily by electrostatic interaction with the substantial partial positive charge of the Fe^{2+} ion. Prominent interactions included metal coordination by negatively charged or polarizable oxygen and nitrogen atoms (e.g., sulfonamide moieties in **PC4** and **PC8**), π–π stacking between aromatic scaffolds and active-site residues such as Phe254, Tyr325, and Trp326, as well as hydrogen-bonding interactions.

To evaluate the stability of the top-ranked binding poses, 500 ns productive MD simulations were performed. RMSD profiles for both protein and ligand are shown in Figures S9 and S10. For the PAH-**PCx** docked complexes, local re-accommodation of the ligands within the active site was frequently observed, yielding apparently more stable conformations over the course of the simulations (Figure S9). **PC5** was the sole exception, displaying continuous transitions between two alternative poses. In all cases, the PAH protein remained structurally stable throughout the simulations. The PAH–**IVx** docked complexes exhibited no significant re-accommodation events, with both protein and ligand RMSD values remaining stable over the entire simulation time (Figure S10). Overall, these simulations indicate that most of the evaluated compounds form stable complexes coordinated to the catalytic ion. The PDB files of the PAH–**PCx** and PAH–**IVx** complexes, obtained after docking and MD refinement are available at the Zenodo repository (https://zenodo.org/records/15825008). It should be stressed that these binding models are based on docking and MD simulations and therefore represent plausible structural hypotheses rather than experimentally validated conformations.

2.6. Toxicity evaluation of chaperones in HepG2 and HEK293T cells

The low toxicity of **PC12** and **PC13** in HepG2 cells has been reported

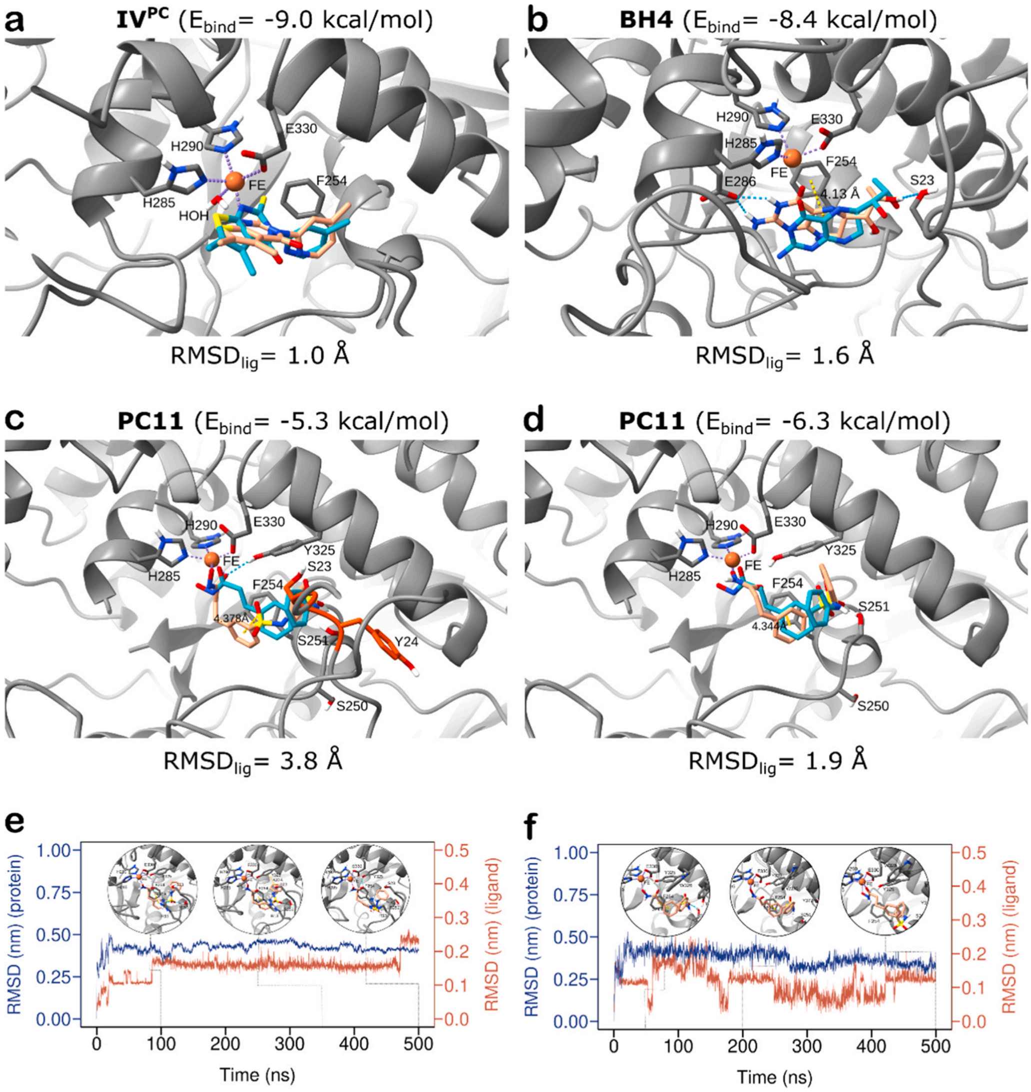

Fig. 4. Best redocked poses obtained by molecular docking for IV^{PC}, BH_4 and belinostat (PC11), and RMSD plots over the 500-ns MD trajectories generated. a) Best redocked pose of $\mathbf{IV^{PC}}$ obtained from rigid docking with AD Vina (sticks, carbons in tan) aligned with its crystallographic pose (sticks, carbons in cyan) from PDB entry 4ANP. b) Best redocked pose of BH_4 obtained from rigid docking with AD Vina (sticks, carbons in tan) aligned with its crystallographic pose (sticks, carbons in cyan) from PDB entry 6HYC. c) Best redocked pose of **belinostat (PC11)** (obtained with AD Vina and the AD4 scoring function from rigid docking on the PAH model without water coordinated to the Fe^{2+} metal ion) (sticks, carbons in tan) aligned with its crystallographic pose (sticks, carbons in cyan) from the **belinostat**-PAH complex structure reported here (PDB ID 9T1O). The N-terminal loop segment of our PAH model including residues Ser23 and Tyr24 is highlighted (orange) to illustrate how it likely prevents a closer match to the crystal pose due to steric clashes. d) Same as in panel c, but showing the best re-docked pose of **belinostat** obtained from flexible docking (side chains of S250, S251 and Y325) with Vina, after removal of the PAH N-terminal segment comprising residues up to Gly33. The calculated binding energies of the re-docked poses and the RMSD of the ligand relative to its crystallographic pose are shown above and below each panel, respectively. Binding energies obtained from Vina scoring function ($\mathbf{IV^{PC}}$ and $\mathbf{BH_4}$) and AD4 scoring function (**belinostat**) are not directly comparable. The coordinated Fe^{2+} ion is depicted as an orange sphere. Hydrogen bonds are illustrated as cyan dashed lines, potential π-stacking interactions as yellow dashed lines (with indicated distances), and coordination bonds to Fe^{2+} as purple dashed lines. e) RMSD plots for the protein (blue line; left y-axis) and **belinostat (PC11)** (wine-red line; right y-axis) for the system initialized from the best rigid-receptor docking pose. f) Same as in panel e but for the system initialized from the best flexible-receptor docking pose. RMSD values were calculated using the gmx rms tool from the GROMACS software, and the plots generated with a custom R script. Circular insets show the binding pose of **belinostat** (sticks with carbon atoms in tan) at selected time frames (indicated with thin grey lines). PAH is shown as a grey cartoon, the Fe^{2+} ion as an orange sphere, and coordinated or interacting residues as sticks with grey-coloured carbon atoms.

previously [23]. To define non-cytotoxic concentration ranges for cellular assays, HepG2 and HEK293T cells were incubated with increasing concentrations of $\mathbf{IV^{PC}}$, its analogues (**IVa**, **IVc–e**, **IVg**, **IVi**, **IVm–q**), **PC1–10**, and **belinostat**. HepG2 cells were treated with concentrations ranging from 25 μM to 1 mM (Figures S11 and S12), whereas HEK293T cells were exposed to concentrations between 25 and 500 μM. These ranges allowed identification of compound concentrations preserving ≥ 90% cell viability, a prerequisite for subsequent efficacy assays in transfected HEK293T cells (Figures S13 and S14). $\mathbf{IV^{PC}}$ analogues exhibited minimal cytotoxicity in HepG2 cells, with most showing CC_{50} values exceeding 1 mM; only **IVn** and **IVo** displayed measurable toxicity, with CC_{50} values of 800 ± 50 μM and 630 ± 60 μM, respectively. **PC1–10** and **belinostat** showed a broader range of cytotoxic responses consistent with their greater chemical diversity. **PC1**, **PC2**, **PC5**, **PC7**, **PC9**, and **PC10** showed no detectable toxicity at the highest concentrations tested (1 mM for **PC1**, **PC2**, **PC5**, **PC7**, and **PC9**; 500 μM for PC10). **PC6** and **PC8** displayed cytotoxic effects only at high concentrations, with CC_{50} values of 927 ± 83 μM and approximately 1 mM, respectively. **PC3**, **PC4**, and **belinostat** exhibited moderate cytotoxicity, with CC_{50} values of 452 ± 17, 407 ± 7, and 370 ± 58 μM, respectively.

In HEK293T cells, most compounds showed no detectable toxicity at the highest concentration tested (500 μM). Measurable cytotoxicity was limited to a small subset of compounds, including **IVo** (CC_{50} ~500 μM), **PC3** (cell viability reduced to 65–70% at 300–500 μM), **PC4** (CC_{50} = 363 ± 10 μM), **PC7** (CC_{50} = 51 ± 1 μM), and **PC8** (CC_{50} = 480 ± 238 μM). All compound concentrations used in subsequent cellular efficacy assays were below those associated with detectable cytotoxicity.

2.7. Variant-dependent chaperoning efficacy in HEK293T cells expressing PKU-associated PAH variants

Using compound concentrations that preserved cell viability, the chaperoning efficacy of all known PAH-stabilizing compounds—including IV^{PC} [20], its rationally designed derivatives [22], previously reported chaperones (**PC12–13**) [23], newly identified hits (**PC1–10**), and **belinostat** (**PC11**)—was assessed in HEK293T cells transiently expressing either wild-type PAH or one of eight pathogenic missense variants (I65T, R241H, V245L, E280K, A395P, V388M, R408Q and Y414C). These variants span the three structural domains of PAH and represent a range of PKU phenotypes with distinct sensitivities to **BH_4** (Figure S15 and Table S7). In many cases, treatment increased the amount of immunoreactive PAH protein while concomitantly decreasing enzymatic activity (Figure S16). A plausible explanation is the inhibitory effect expected for stabilizing compounds that bind within the catalytic site [41], particularly at high concentrations, where inhibition may obscure chaperoning activity. For instance, **IVi** and **belinostat** markedly reduced PAH enzymatic activity at the highest concentration tested (Figure S17). Accordingly, to identify, for each compound, the concentration that maximized PAH enzymatic activity, dose–response assays were performed at 0.1, 1, 10, 50, 100, and 200 μM in cells expressing wild-type PAH. Based on these analyses, the following concentrations were selected for subsequent variant-specific efficacy assays: 0.1 μM (**IVd**, **IVp**, **PC1**, **PC2**, **PC3**, **PC8** and **PC9**), 1 μM (**IVc**, **IVe**, **IVi**, **IVn**, **PC5**, **PC6**, **PC7**, **PC10** and **PC13**), 10 μM (**IVa**, **IVo**, **PC4** and **belinostat**), 50 μM (**IVg**), 100 μM (**IV^{PC}** and **IVm**), and 200 μM (**IVq** and **PC12**).

Fold-changes in PAH protein levels and enzymatic activity for all variants treated with each compound at the selected concentrations are provided in Figures S18–S26. A global comparison of compound effects, summarized in the heat maps of Fig. 5, reveals distinct patterns of potency and specificity. All tested molecules increased PAH activity in at least one cell line expressing a PAH variant. Several compounds

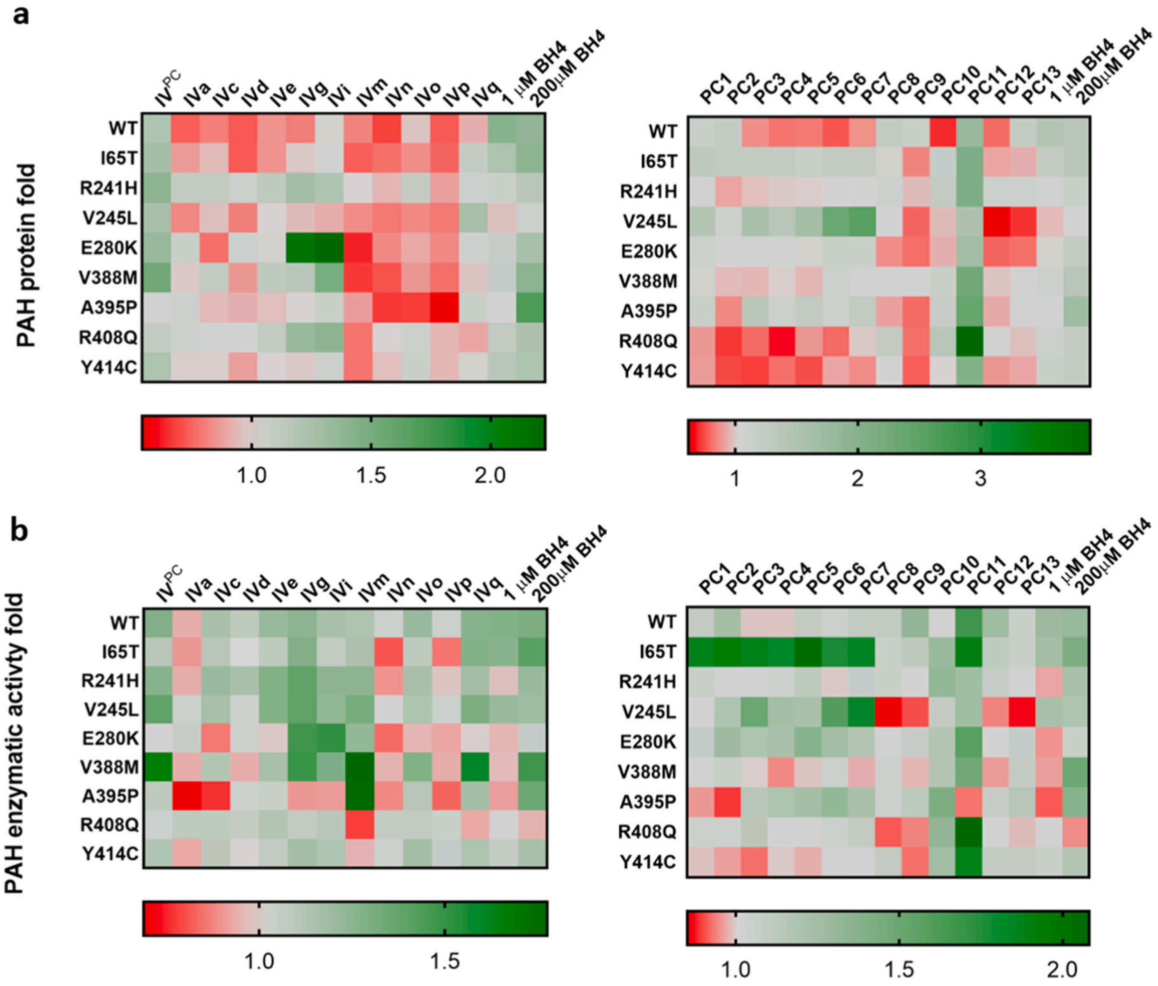

Fig. 5. Heat maps summarizing compound effectiveness in cells expressing wild-type PAH or pathogenic variants. (**a**) Immunoreactive PAH protein levels and (**b**) PAH enzymatic activity levels determined for HEK293T cells treated with the evaluated compounds. Protein levels are the average of three independent assays with two technical replicates (n = 6), while activity levels are the average of three independent assays (n = 3). In a few cases, (see Fig. S19, S22, S23, S26 and S27 legends) protein or activity levels are the average of two independent assays (n = 4 or n = 2, respectively). Heat map values represent mean relative PAH protein levels or enzymatic activities of cells expressing wild-type PAH or 8 different pathogenic variants after treatment with each of the 26 evaluated compounds, relative to untreated control cells. As indicated by the colour scale, values equal to 1 are coloured in grey; values above 1 are coloured in progressively darker green up to the maximum value; and values below 1 are coloured in progressively darker red down to the minimum value obtained. Statistical analysis of the underlying measurements is provided in Tables S8–S11, where p-values and statistical significance (Student's *t*-test) are indicated in parentheses.

produced minimal effects across the tested variants (**PC8**, **PC13**, **IVa**, **IVc**, **IVd**, **IVn**, and **IVp**), whereas others increased activity only in cells expressing wild-type PAH **(PC9** and **PC12)**. Two compounds showed only modest effects limited to a small number of variants. (**IVe** in R241H and V245L; **IVo** in V388M). **PC10** increased activity across all variants tested, although it was never the most effective compound for any specific variant. Several compounds emerged as the most effective chaperones for specific PAH variants. **PC1**, **PC2**, **PC4**, and particularly **PC5**, showed the strongest rescue on the I65T variant. **PC3**, **PC6**, and **PC7** also markedly improved I65T activity and, in addition, enhanced PAH activity in the V245L variant. **IV^{PC}**, **IVq**, and **IVm** were the most effective chaperones for V388M, the latter compound being also the most active for A395P. **IVg** displayed efficacy across several variants and was the top-performing compound for R241H. **Belinostat** (**PC11**) was the most effective chaperone for E280K, R408Q, and Y414C, and also showed substantial activity for I65T and V388M, while having no detectable effect on A395P.

When the same data are organized by PAH variant rather than by compound, clear differences in cellular response become apparent. I65T was efficiently targeted by many of the newly identified chaperones (**PC1–7**) and by **PC11**, most of these compounds nearly doubling PAH activity. In contrast, **PC8–10**, **PC12**, **PC13**, and **IV^{PC}** (together with its derivatives) produced minimal effects on this variant. The R241H variant responded weakly to most compounds, with **IVg** achieving the highest effect (1.4-fold increase). V245L was most effectively chaperoned by **PC7** (1.8-fold increase), followed by **PC6** and **PC3**. For the E280K variant, **PC11**, **IVg**, and **IVi** produced similar 1.5-fold increases in PAH activity. In V388M-expressing cells, activity was enhanced by **PC11**, **IV^{PC}**, **IVg**, and **IVq**, and most prominently by **IVm** (1.8-fold increase). In A395P, **IVm** was also the most effective compound (1.8-fold increase) with **PC10** also exerting a significant effect. Finally, the R408Q and Y414C variants were only rescued by **PC11** (2.1- and 1.9-fold increases, respectively). **PC12** and **PC13**, which were previously reported to reduce blood L-Phe levels in a PKU mouse model [23], showed little to no increase in PAH activity for any of the PAH variants tested under our cellular assay conditions. Taken together, these results define a variant-specific efficacy landscape that can be directly compared with the response to tetrahydrobiopterin.

2.8. Cellular efficacy of tetrahydrobiopterin across PKU-associated PAH variants in the same assay

Tetrahydrobiopterin (**BH_4**), the natural PAH cofactor, is the only approved pharmacological chaperone for PKU and lowers blood phenylalanine levels in a subset of patients by acting as a pharmacological chaperone for certain PAH variants [13,42]. Reported clinical response data for homozygous carriers of the variants examined in this study, as compiled in BIOPKUdb (last accessed on March 21, 2025), are summarized in Table S7. The efficacy of tetrahydrobiopterin was assessed in the same cellular assay using identical experimental readouts. In our cellular assay, **BH_4** failed to increase PAH activity in E280K- or R408Q-expressing cells and produced only modest activity increases (~1.2-fold) in R241H, V245L, and Y414C. Its strongest effects—approximately 1.4-fold increases—were observed for I65T, V388M, and A395P. A comparative overview of **BH_4** performance relative to the remaining chaperones is shown in Fig. 6. Across the tested PAH variants, **BH_4** did not rank as the top-performing compound for any variant. For each PAH variant, the best-performing chaperone, its fold improvement relative to **BH_4**, and the **BH_4** rank among the 26 PCs tested are as follows. For I65T: **PC5** (+1.4-fold relative to **BH_4**; **BH_4** ranked 9th). For R241H: **IVg** (+1.1-fold; **BH_4** ranked 8th). For V245L: **PC7** (+1.5-fold; **BH_4** ranked 13th). For E280K: **PC11** (+1.5-fold; **BH_4** ranked 15th). For R408Q: **PC11** (+2.1-fold; **BH_4** ranked 20th). For Y414C: **PC11** (+1.6-fold; **BH_4** ranked 5th). For V388M: **IVm** (+1.2-fold; **BH_4** ranked 5th). For A395P: **IVm** (+1.3-fold; **BH_4** ranked 3rd). These comparisons show that multiple pharmacological chaperones outperform **BH_4** in a variant-dependent manner in the same cellular assay.

3. Discussion

Pharmacological chaperones are small molecules that modulate protein folding, stability, or assembly within the intracellular environment, thereby influencing the abundance of functional protein species. Using identical cellular readouts for all compounds, we observed a broad spectrum of functional responses. A substantial subset of compounds (**PC8**, **PC9**, **PC12**, **PC13**, **IVa**, **IVc**, **IVd**, **IVn**, and **IVp**) produced only minor changes in PAH activity across the tested variants (Tables S8 and S9), with increases not exceeding 20%. Their effects on PAH protein levels were similarly modest (Tables S10 and S11). Although these molecules form stabilizing complexes with wild-type PAH in vitro, they do not elicit a substantial chaperoning effect in cells, suggesting limited effective exposure or engagement under the cellular assay conditions. In contrast, the remaining compounds (**IV^{PC}**, **IVe**, **IVg**, **IVi**, **IVm**, **IVo**, **IVq**, **PC1–7**, **PC10**, and **belinostat**) produced clear increases in PAH activity under the same conditions, indicating measurable cellular rescue. Importantly, their maximal efficacy was strongly variant-dependent:

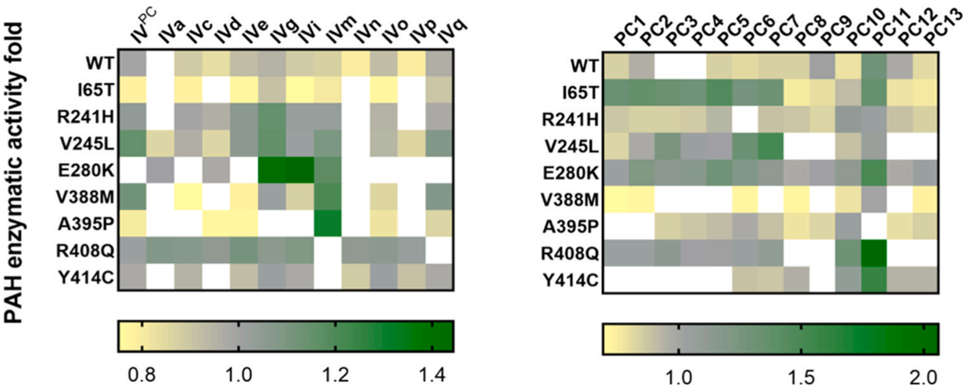

Fig. 6. Relative PAH-chaperoning effects of the evaluated compounds, compared with **BH_4.** The PAH enzymatic activity levels of HEK293T cells treated with the evaluated compounds are represented relative to those of cells treated with **BH_4**. Heat maps represent the ratio between the mean PAH enzymatic activity values for each compound treatment and those obtained in the presence of 1 μM **BH_4** (for V245L and R408Q variants) or 200 μM **BH_4** (for the remaining variants). The colour scale indicates the association between the ratios and the represented colours: ratio of 1 (grey), ratio above 1 (green, gradually from grey to green up to the maximum value) and ratio below 1 (light yellow, gradually from grey to yellow down to the minimum value). Uncoloured cells correspond to compound–variant combinations for which treatment did not produce an increase in PAH enzymatic activity relative to untreated cells. Statistical analysis of the underlying activity measurements is provided in Tables S8–S9.

PC5 was most effective for I65T; **IVg** for R241H; **PC7** for V245L; **belinostat** (**PC11**) for E280K, R408Q, and Y414C; and **IVm** for both V388M and A395P. Notably, **BH$_4$** was not the most effective compound for any of the variants examined. Given that **PC7** shows toxicity in HEK293T cells, **PC6** or **IVg** may offer safer alternatives for targeting V245L. For chronic metabolic disorders such as PKU, long-term therapy requires compounds with favorable pharmacokinetic properties and convenient routes of administration. In this context, **PC5**, **PC6**, **PC11** (Figure S1), **IVg**, and **IVm** [22] are predicted to have high intestinal absorption and a low likelihood of crossing the BBB, features that are desirable for therapeutic development. The diversity of variant-specific efficacy profiles and the favorable predicted ADME and toxicity properties of these compounds highlight the feasibility of identifying **BH$_4$**-independent chaperones with differentiated, variant-tailored activities. In the specific case of belinostat, pharmacokinetic data [43,44] indicate that, after standard intravenous dosing (1000 mg/m^2), the estimated free circulating concentration—based on its reported plasma protein binding—is in the low micromolar range, i.e., of the same order of magnitude as the 10 μM used in our chaperoning assays. This suggests that PAH stabilization by belinostat and HDAC inhibition are likely to occur concomitantly at clinically relevant exposures, raising concerns for long-term pediatric treatment. Accordingly, future studies should explore whether PAH stabilization can be achieved at lower concentrations or focus on the development of belinostat derivatives with reduced HDAC inhibitory activity.

To further dissect compound-specific response patterns, we compared PAH enzymatic activity with cellular PAH abundance. Individual PCs exert markedly different effects on cellular PAH levels. For example, the strong chaperoning of V388M by **IV^{PC}**, **IVq**, and **IVm** occurs alongside increased, unchanged, and even reduced PAH protein abundance, respectively. **Belinostat** (**PC11**) typically produces strong chaperoning effects, often manifesting as marked increases in PAH protein levels. However, in certain variants (e.g., A395P), such increases do not lead to higher enzymatic activity, suggesting that, for some variants, PC11 increases the abundance of PAH species that are catalytically incompetent. Conversely, moderate decreases in PAH protein levels occur in some cases without a reduction in enzymatic activity, suggesting that some PCs may enhance the clearance of misfolded or non-productive PAH conformers. Because activity and protein abundance can change independently, these measurements alone cannot distinguish kinetic from thermodynamic chaperoning mechanisms, and, in practice, both mechanisms may contribute in some cases. Nevertheless, the observation that these PCs appear to bind to the same site on native PAH (Fig. 4; Figures S7–S8) with comparable affinities (Fig. 1b), yet display distinct variant-dependent efficacy patterns (Fig. 5), is difficult to reconcile with a solely thermodynamic mechanism. These findings are more consistent with kinetic chaperoning, in which different PCs preferentially bind to and modulate distinct folding intermediates within the multistep PAH folding pathway. Indeed, prior evidence shows that **IV^{PC}** reshapes and accelerates the folding trajectory of PAH [21].

Changes in activity and protein levels can indicate whether a PC enhances the intrinsic catalytic performance of PAH—reflected in its turnover number (TN)—or simply increases the amount of enzyme present. The relative TNs (treated versus untreated cells) of wild-type and PAH variants, shown in Tables S12 and S13, reveal diverse behaviours. For most PCs, the relative TN remains close to 1.0, indicating that they primarily increase the amount of active enzyme without improving its catalytic quality. In the case of **IVm**, however, the relative TN significantly increases for several variants, suggesting enhanced catalytic competence and, consequently, an improvement in protein quality, not just quantity. **Belinostat** exhibits a more complex behaviour. As with most other PCs, its strong, broadly acting chaperoning effect arises from increasing the total amount of active protein. However, for some variants, **belinostat** actually lowers the relative TN, implying that it elevates the levels of both active and inactive species. Belinostat is a histone deacetylase inhibitor [45] and could in principle influence PAH expression through transcriptional or epigenetic mechanisms. The facts that it binds directly to the PAH catalytic site, produces a clear thermostabilizing effect in vitro, and displays variant-dependent rescue profiles in cells argue for a predominantly direct pharmacological chaperoning effect. Nevertheless, we cannot exclude that HDAC inhibition may indirectly contribute to PAH levels through broader effects on cellular proteostasis.

PAH functions as a homotetramer, and it is well established that many pathogenic variants exhibit impaired tetramerization and a propensity to aggregate [46]. To assess whether the observed increases in activity share a common mechanistic outcome, we used mass photometry to quantify the distribution of oligomeric states of wild-type PAH and four representative variants (I65T, V245L, R408Q, Y414C) (Fig. 7a). We then assessed how selected chaperones modify this oligomerization equilibrium (Fig. 7b and Fig. 8) and derived the corresponding changes in the monomeric and tetrameric fractions (Table S14) for the 14 variant–compound pairs that showed a statistically significant increase in enzyme activity (Tables S8 and S9). In every case, increased PAH activity coincided with an increased proportion of tetramer. Although the correlations were moderate—positive for tetramer abundance (Spearman $\rho = 0.57$, $p = 0.011$) and negative for monomer fraction ($\rho = -0.61$, $p = 0.0051$)—they align with the well-established higher catalytic efficiency of tetrameric PAH [47]. While these relationships do not prove that tetramer stabilization is the sole mechanism of action, they indicate that increased tetramer abundance is a common outcome of effective treatment. Several variant-specific examples illustrate this link. In wild-type PAH, the strong increases in tetramerization induced by **BH$_4$**, **PC11** and **IVg** were accompanied by enhanced enzymatic activity (Fig. 7b). For I65T (Fig. 8a), **PC11**, **PC3** and **BH$_4$** similarly produced marked increases in both tetramer abundance and activity. V245L showed an analogous response to **IVg**, **PC4**, **PC6**, **PC3**, and **PC7** (Fig. 8b). For R408Q (Fig. 8c), **PC10** increased both tetramerization and activity, and, for Y414C (Fig. 8d), **IV^{PC}**, **PC10** and **PC11** elicited the same dual effect. These findings indicate that enhanced PAH tetramer formation is a recurring feature of effective pharmacological chaperoning. Pharmacological chaperoning of PAH emerges as both variant- and compound-dependent. At the cellular level, increased PAH activity can arise either from improved catalytic competence, reflected in higher turnover numbers, or from an increased abundance of enzyme. The collected evidence supports a predominantly kinetic chaperoning mechanism and indicates that effective rescue is consistently associated with a shift of the oligomerization equilibrium toward the tetrameric state.

4. Conclusions

Phenylketonuria is a monogenic disorder with marked genotype–phenotype heterogeneity, for which no current pharmacological therapy provides broad clinical coverage. Our results demonstrate that a genotype-guided, “à la carte” strategy based on pharmacological chaperones is feasible. By benchmarking 26 structurally diverse compounds across eight disease-associated PAH variants under identical cellular conditions, we define a strongly variant-dependent efficacy landscape in which multiple compounds outperform tetrahydrobiopterin (BH$_4$). Despite their chemical diversity, effective chaperones converge on a shared mechanistic outcome: increased formation of tetrameric, catalytically active PAH. These findings provide a preclinical proof-of-concept for precision pharmacochaperone therapy in PKU and establish a rational framework for the development and optimization of variant-targeted treatments.

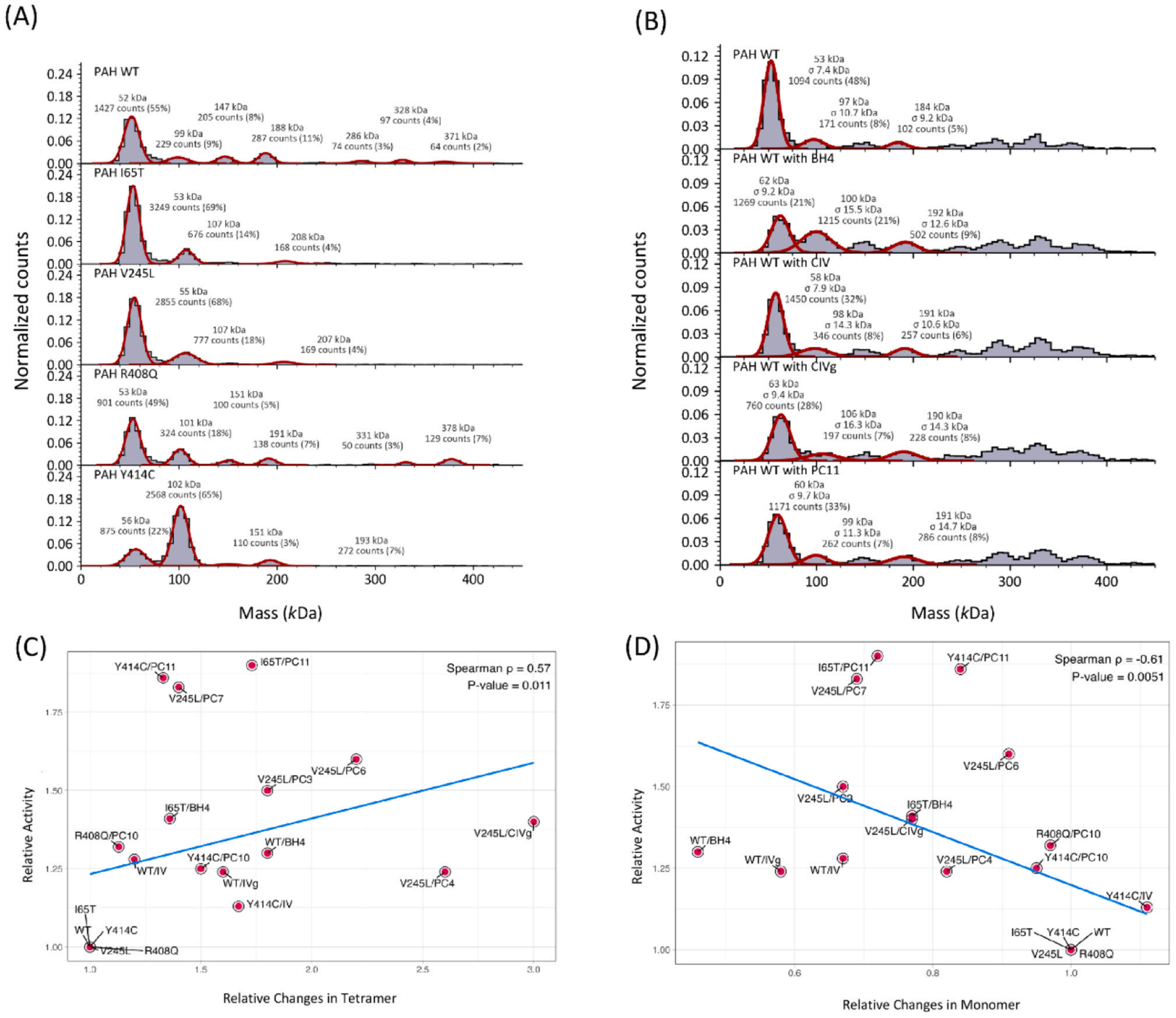

Fig. 7. Association of structural dispersity and enzymatic efficiency. (a) Oligomeric distribution of wild-type PAH and pathogenic variants determined by mass photometry. (b) Changes in oligomeric distribution of wild-type PAH following treatment with selected pharmacological chaperones that improved enzymatic function. (c) Correlation between relative changes in tetramer abundance and enzymatic activity. (d) Correlation between relative changes in monomer abundance and enzymatic activity. Spearman's correlation coefficients (ρ) and corresponding p-values are indicated in the plots.

5. Materials and methods

5.1. Reagents and chemicals

The Prestwick Chemical Library (Prestwick Chemical) and the Hit-Finder Collection (Maybridge Ltd) were screened to identify potential new drugs for the treatment of PKU. The first collection consisted of 1120 FDA-approved drugs. The second collection consisted of 10,000 compounds selected for their chemical diversity, all of them complying with Lipinski's guidelines for drug-likeness. The ten newly identified hits (**PC1–10**) were subsequently purchased from Maybridge Ltd. Eleven analogues of compound **IV^{PC}** (**IVa, IVc-e, IVg, IVi and IVm-q**) were synthesized as described [22]. **5-benzylhydantoin** and **5-benzylidene-2-thiohydantoin** (here termed **PC12–13**) were purchased from Sigma-Aldrich. **BH$_4$** was purchased from Sigma Aldrich. **Belinostat** (hereafter also termed **PC11**) was purchased from Selleck Chemicals LLC. All compounds were dissolved in 100% dimethyl sulfoxide (DMSO) and stored frozen at −20 °C. The chemical structures of the 26 compounds tested in HEK293T cells for chaperoning efficacy are shown in Table 1 (new compounds **PC1-10**) and Table S6.

5.2. Expression and purification of human recombinant PAH

Two constructs designed to obtain either the full-length tetrameric form of the enzyme (PAHt) or a truncated dimeric form lacking the regulatory domain and the C-terminal tetramerisation helix (PAHd) were expressed in *E. coli* BL21 (DE3) cells. In both constructs, PAH was expressed as a fusion protein with maltose-binding protein (MBP) at the N-terminus. PAH was purified using amylose affinity chromatography, a protease cleaving step, consecutive amylose and glutathione affinity chromatography and a final size-exclusion step [21,28]. For the mass photometry experiments, wild-type PAH and its pathogenic variants were expressed and purified using the same procedure, but omitting the size-exclusion chromatography step. Some disease-associated mutations are known to show impaired tetramer assembly. Omitting the indicated step allowed direct observation of their structural behaviour in solution, with and without PCs.

5.3. High-throughput screening (HTS)

The Maybridge Hit Finder Collection and the Prestwick Chemical

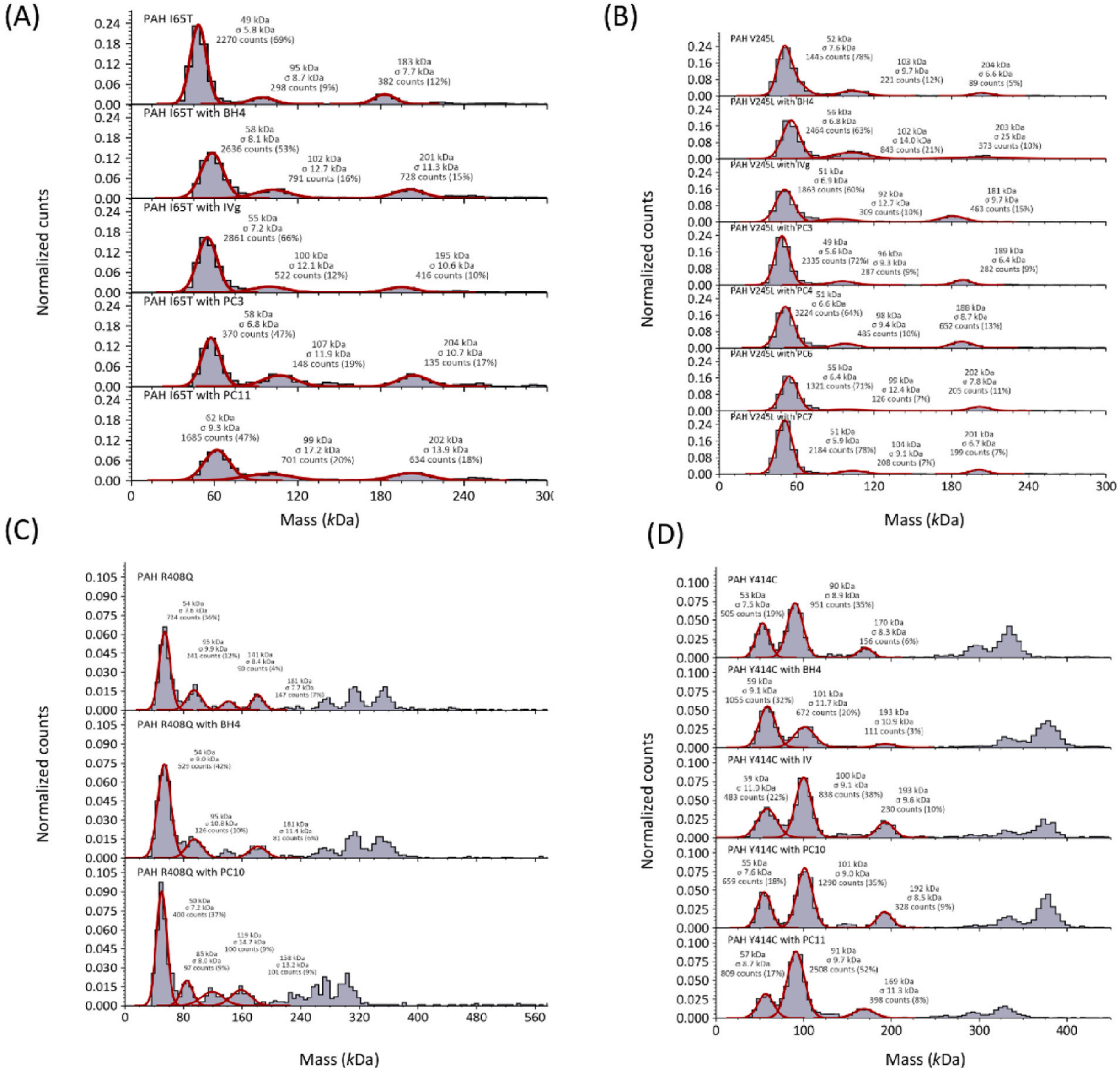

Fig. 8. Changes in PAH oligomeric distribution following pharmacological chaperone treatment. Structural dispersity changes in PAH variants upon treatment with selected pharmacological chaperones that resulted in increased enzyme activity. Oligomeric distributions were determined by mass photometry. (a) I65T, a mutation in the regulatory domain, (b) V245L, a mutation in the catalytic domain, (c) R408Q, a mutation in the tetramerization domain, (d) Y414C, another mutation in the tetramerization domain. For comparison, the effect of BH_4 is shown for all the variants.

Library were screened by monitoring the thermal denaturation of wild-type recombinant PAH in the presence of each of the compounds tested. For this purpose, the fluorescence of the extrinsic ANS probe was measured in a FluoDia T70 High-temperature Fluorescence Microplate Reader (Photon Technology International) by exciting at 390 nm and collecting the emission at 500 nm. A temperature ramp of 1 °C/min was used from 20 to 70 °C with an equilibration time of 1 min at each temperature before measurement. Protein solutions (100 µL containing 5 µM PAHt, 20 mM Tris (pH 7.4), 200 mM NaCl, 250 µM ANS and either 100 µM of HitFinder or 250 µM of Prestwick compound) were dispensed into 96-well microplates and covered with 50 µL of mineral oil. To speed up the screening, in a first round, four compounds were placed in each well. As the compounds were dissolved in 100% DMSO, the final concentration of DMSO in the wells was 10%. In each microplate, 16 wells containing 10% DMSO but no compound added were used as control. Unfolding PAH curves were analysed with Origin 7 (OriginLab). In previous work, we reported that the PAH thermal unfolding is three-state [28]. For the present HTS, the two transitions described were not taken into account. Instead, an apparent temperature of mid denaturation, T_m, was calculated as the inflection point of the unfolding curve, corresponding to the temperature at which the curve has its steepest slope. Ligands binding to PAH exert a thermostabilising effect which is manifested by an increase in the apparent T_m. Positive hits were defined as wells whose T_m^{hit} exceeded the mean T_m of control wells of the same microplate by more than three times its standard deviation (Eq. 1):

$$T_m{}^{hit} \geq \quad T_m{}^{control} \quad + 3 \times SD \tag{1}$$

In a second round of screening, each of the 4 compounds present in any positive well was individually evaluated using control wells containing 2.5% DMSO instead of 10%.

5.4. Conventional thermal denaturation analysis

Validation of the hit compounds found was performed using a real-time qPCR Stratagene Mx3005P thermocycler (Agilent Technologies) with an ANS fluorescence filter. Protein-ligand samples contained 5 µM

PAHt in 20 mM Tris, pH 7.4, 200 mM NaCl, 250 μM ANS, 100 μM of the hit compound and 2.5% DMSO. Thermal unfolding curves were individually fitted to a three-state unfolding model, as described [48], using Eq. 2:

$$F = \frac{(F_N^o + m_N \times T) + (F_I^o + m_I \times T) \times e^{-(\Delta G_1)/R \times T} + (F_U^o + m_U \times T) \times e^{-(\Delta G_1 + \Delta G_2)/R \times T}}{1 + e^{-(\Delta G_1)/R \times T} + e^{-(\Delta G_1 + \Delta G_2)/R \times T}} \tag{2}$$

where F_N^o, F_I^o and F_U^0 are the fluorescence intensity signals of the native, intermediate and unfolded states at 0 K, respectively, m_N, m_I (set to zero in the fit), and m_U are the corresponding slopes of their linear temperature dependencies, ΔG_1 and ΔG_2 the unfolding Gibbs energy changes of the two transitions and R is the universal gas constant. The above Gibbs energy changes (ΔG_i) are related to the enthalpy changes (ΔH_i) and heat capacity changes (ΔC_{pi}) of the corresponding equilibria and their transition temperatures (T_{mi}) by Eq. 3:

$$\Delta G_i\,(T) = \Delta H_i\,(T_{mi}) \times \left(1 - \frac{T}{T_{mi}}\right) + \Delta C_{pi} \times \left[T - T_{mi} - T \times \ln\left(\frac{T}{T_{mi}}\right)\right] \tag{3}$$

The thermal shifts (ΔT_{mi}) associated with a compound are calculated by Eq. 4:

$$\Delta T_{mi} = T_{mi}{}^{hit} - T_{mi}{}^{control} \tag{4}$$

5.5. Isothermal titration calorimetry (ITC)

The binding affinity of hit compounds **PC1–10** and **belinostat** for PAH was measured in a MicroCal Auto-iTC200 (MicroCal, Malvern Panalytical). The PAHt (20–50 μM monomer concentration in PBS, pH 7.4) and hit compound (300–1200 μM, dissolved in the same buffer) solutions were degassed and loaded into the cell and syringe, respectively. The working compound solutions were prepared from stocks in 100% DMSO and contained the same residual DMSO concentration (2.5%). Titrations were performed at 25 °C by injecting 2 μL of ligand solution into the sample cell every 150 s. A one-site binding model implemented in the Origin 7.0 software (OriginLab) was used to analyse the data and obtain the thermodynamic parameters [49].

5.6. Crystallization of the PAH-belinostat complex

The recombinant truncated form of the enzyme (dimeric PAH, hereafter PAHd) was used to obtain crystals at 4 °C by the hanging-drop vapour diffusion technique, in 24-well plates. 1 μL of PAHd solution (10 mg/mL in 20 mM Tris, pH 7.4, 200 mM NaCl) was mixed with one μL of mother liquor (40 mM PIPES, 18% PEG 2000, pH 6.5) and equilibrated with 500 μL of mother liquor in the reservoir. After 1–2 weeks, the protein crystals were soaked with 20 mM **belinostat** (10% DMSO) in mother liquor solution and equilibrated overnight in the same reservoir. The soaked crystals were cryoprotected in mother liquor solutions containing 25% ethylene glycol and frozen in a stream of nitrogen gas cooled to 100 K.

5.7. X-ray data collection and refinement

Diffraction data were collected at the I03 synchrotron beamline of the Diamond Light Source (Harwell Science and Innovation Campus, Oxfordshire, UK). Diffraction patterns were processed and scaled using the XDS package [50] and the CCP4 software [51]. The structure of the PAHd-**belinostat** complex was solved by molecular replacement with MOLREP [52] using PDB ID 4ANP as the template [21]. Initial phases were improved through iterative cycles of manual model building in Coot [53], alternated with restrained refinements in REFMAC5 [54], followed by final TLS-restrained refinement. The final model of PAHd complexed with **belinostat** was validated with PROCHECK [55]. Relevant statistics are given in Table S5.

5.8. Modelling of PAH-ligand interactions

The molecular interaction between PAH and compounds **PC1-PC13**, **IV^{PC}, IVa, IVc-e, IVg, IVi** and **IVm-q** was modelled with AutoDock Vina [56,57]. The high-resolution but incomplete PAH structure from PDB entry 6N1K [40] served as the initial template for modelling the complete tetrameric assembly. The unresolved regions of 6N1K—most notably the C-terminal tetramerization helix, but also short internal segments—were modelled by structurally superimposing the AlphaFold 2 PAH model (monomer) and incorporating the missing regions. The Cys29Ser mutation present in the original structure was reverted to the wild-type amino acid. Protonation state assignment, parameterization of the PAH metal coordination environment and generation of PDBQT files are described in the Supplementary Material **(Methods** and Figure S27). Rigid and flexible re-docking and docking experiments, details on the specific model used for the flexible re-docking of **belinostat** and assessment of convergence is also described in the Supplementary Material. Docking poses were ranked with both the default Vina scoring function [56] and the AutoDock4 scoring function [58]. To assess the stability of the best docked poses, 500-ns molecular dynamics (MD) productive simulations (NPT ensemble) were performed using the GROMACS package (v.2025.1) [59], following appropriate system preparation and equilibration. RMSD values for the receptor and ligand (RMSD_lig) were calculated across the resulting productive trajectories using the *gmx rms* tool from GROMACS. Further details on the simulation setup and parameters are provided in the Supplementary Material.

5.9. Cell line cultures

HepG2 and HEK293T cell lines (ATCC) were used to assess compounds toxicity while their efficacy was studied in HEK293T cells overexpressing wild-type PAH or PAH variants. HepG2 cells were grown in Minimum Essential Medium (MEM) containing 0.292 g/L glutamine (Thermo Fisher Scientific), 10% FBS (PAN-Biotech GmbH), 100 U/mL penicillin and 100 μg/mL streptomycin (PAN-Biotech GmbH). Similarly, HEK293T cells were cultured in Dulbecco's Modified Eagle Medium (DMEM) containing 4.5 g/L glucose and 0.584 g/L glutamine (Sigma-Aldrich), 10% FBS, 100 U/mL penicillin and 100 μg/mL streptomycin.

5.10. Toxicity of compounds in cell culture

In a 96-well plate, 90 μL of cells were seeded at a density of 3×10^5 cells/mL in DMEM or MEM without phenol red, 10% FBS, 100 U/mL penicillin and 100 μg/mL streptomycin, and grown at 37 °C in a 5% CO_2 atmosphere for 24 h. Compounds were added at different concentrations, maintaining a final DMSO concentration of 1% in each well. Cells were incubated with the compounds for 24 h. Control wells, representing 100% viability, contained cells seeded at the same density and incubated with 1% DMSO but no compound. Cell viability in treated and control wells was measured by the 2,3-bis-(2-methoxy-4-nitro-5-

sulphenyl)-(2 H)-tetrazolium-5-carboxanilide (XTT) method (Cell Proliferation kit II, Roche), according to the manufacturer's protocol. Absorbance at 450 and 650 nm were recorded in a Synergy HT microplate reader (Biotek) and the percentage of cell viability was calculated, using Eq. 5:

$$\%cell\ viability = \frac{(\mathrm{Abs}_{450} - \mathrm{Abs}_{650})\mathrm{compound} - (\mathrm{Abs}_{450} - \mathrm{Abs}_{650})\mathrm{XTT}}{(\mathrm{Abs}_{450} - \mathrm{Abs}_{650})\mathrm{control} - (\mathrm{Abs}_{450} - \mathrm{Abs}_{650})\mathrm{XTT}} \times 100 \tag{5}$$

The 50% cytotoxic concentration (CC_{50}), defined as the compound concentration at which cell viability is halved, was calculated by fitting the cell viability at different compound concentrations to a dose-response Hill function implemented in Origin 8.0 (OriginLab).

5.11. Effects of compounds on the protein level and enzymatic activity of PAH variants transiently expressed in HEK293T cells

HEK293T cells were seeded in 24-well plates at a density of 2.2×10^5 cells/mL in DMEM medium supplemented with 10% FBS and without antibiotics. After 24 h, the cells were transfected with 0.5 μg of pcDNA3.1 +N-DYK-PAH (wild-type or mutant constructs) plasmid DNA (GenScript) per well and 2 μL Lipofectamine 2000 (Thermo Fisher Scientific), as described by the manufacturer. Five hours after transfection, compounds were added and the cells were incubated for 24 h, harvested and stored at −80 °C. The effectiveness of the 6R-$\mathrm{BH_4}$ natural cofactor (Sigma Aldrich) was compared with that of the 10 newly identified hit compounds (**PC1–10**), the previously reported compound **IV^{PC}** [20] and 11 computationally designed derivatives (**IVa, IVc-e, IVg, IVi and IVm-q**) [22], **belinostat** (renamed as **PC11**), and the reported [23] PAH pharmacological chaperones **5-benzylhydantoin** (Sigma Aldrich) and **5-benzylidene-2-thiohydantoin** (Sigma Aldrich) (renamed as **PC12** and **PC13**, respectively). Each compound was evaluated at a concentration that guaranteed a cell viability above 90% and a lack of inhibitory effect on the enzymatic activity. The selected concentrations were 0.1 μM for **IVd**, **IVp**, **PC1**, **PC2**, **PC3**, **PC8** and **PC9** treatment; 1 μM for **IVc**, **IVe**, **IVi**, **IVn**, **PC5**, **PC6**, **PC7**, **PC10** and **PC13** treatment; 10 μM for **IVa**, **IVo**, **PC4** and **belinostat** treatment; 50 μM for **IVg** treatment; 100 μM for **IV^{PC}** and **IVm** treatment, and 200 μM for **IVq** and **PC12** treatment. Two different treatment concentrations were used for **$\mathrm{BH_4}$** effectiveness evaluation depending on the PAH variant expressed: 1 μM **$\mathrm{BH_4}$** for the V245L and R408Q variants and 200 μM **$\mathrm{BH_4}$** for the rest of variants. Both treatment and control wells contained 0.2% DMSO.

PAH protein levels were measured by Western blot (WB). Cell pellets were lysed in 20 mM Tris, pH 7.4, 200 mM NaCl, 1 mM DTT, 1% (v/v) Triton X-100, 1 mM benzamidine, 100 μM leupeptin and 200 μM phenylmethylsulfonyl fluoride. After centrifugation, the total protein concentration was determined by the bicinchoninic acid method. Cell extract samples were loaded (7.5–15 μg of total protein per well) in 10% SDS-PAGE gels and subsequently transferred to a polyvinylidene difluoride Immobilon-P membrane (Millipore). Immunoblotting was done with two horseradish peroxidase (HRP)-conjugated antibodies: the DYKDDDDK tag monoclonal mouse antibody [HRP] (GenScript) and the glyceraldehyde 3-phosphate dehydrogenase (GAPDH) polyclonal goat antibody [HRP] (GenScript). The tag antibody allowed for PAH detection and the GAPDH antibody was used as a loading control in WB. Finally, chemiluminescence detection was carried out by Immobilon Western Chemiluminiscence HRP Substrate (Millipore) with a ChemiDoc MP Imaging System (Bio-Rad). PAH expression with compound treatment was quantified, relative to expression controls, using Image Lab software (Bio-Rad). Relative PAH protein levels were calculated using Eq. 6:

$$relative\ PAH\ protein\ level = \frac{\left(\frac{\mathrm{DYK-PAH\ signal}}{\mathrm{GAPDH\ signal}}\right) with\ compound}{\left(\frac{\mathrm{DYK-PAH\ signal}}{\mathrm{GAPDH\ signal}}\right) in\ control} \tag{6}$$

PAH activity on cell extracts transiently expressing the enzyme was measured at 37 °C for 30 min by HPLC-quantification of the L-Tyr product formed. PAH activity reactions were carried out with 30–60 μg of total protein preincubated for 4 min at 37 °C in 200 mM Tris, pH 7.2, 1 mg/mL catalase (Sigma Aldrich), 1 mM L-Phe (Sigma Aldrich) and 0.5% (w/v) BSA (Fisher Scientific). After this initial preincubation, 100 μM ferrous ammonium sulfate (Sigma Aldrich) was added and the reaction was started after 1 min by adding 200 μM 6R-$\mathrm{BH_4}$ (Sigma Aldrich) and 5 mM dithiothreitol (Sigma Aldrich). After 30 min, the reaction was stopped by incubating the samples at 100 °C for 5 min. Reaction samples were centrifuged and the supernatant loaded onto a modular HPLC Alliance system (Waters). Product separation was made with a XSelect HSS T3 column (Waters) and 25% methanol (v/v) solution as mobile phase. Product formation was quantified by fluorescence emission at 302 nm (λ_{exc} 210 nm). The chromatograms were analysed with the Empower 3 software (Waters) and the Tyr formed was quantified using a standard curve. The increase in PAH activity (relative PAH activity level) was calculated as the enzymatic activity of the samples treated with compound relative to that of the control samples using Eq. 7.

$$relative\ PAH\ activity\ level = \frac{(\mathrm{PAH\ activity})with\ compound}{(\mathrm{PAH\ activity})in\ control} \tag{7}$$

Finally, the turnover number (TN) of PAH enzyme molecules in treated cells, relative to that in untreated ones was calculated with Eq. (8):

$$relative\ TN = \frac{relative\ PAH\ activity\ level}{relative\ PAH\ protein\ level} \tag{8}$$

5.12. Effects of compounds on the PAH oligomerisation equilibrium

Microscope coverslips (No. 1.5, sizes 24 × 50 and 24 × 24 mm, VMR) were cleaned by sequential sonication for 5 min each in 50% isopropanol (HPLC grade)/Milli-Q water, followed by pure Milli-Q water. They were then dried using a clean nitrogen stream. A six-well silicone mold was placed on top of the coverslips to create the sample chambers. Prior to mass photometry, protein samples were diluted to 200 nM in 20 mM Tris, 200 mM NaCl, pH 7.4. Each measurement was performed in a new sample chamber. The chamber was initially filled with 19 μL of fresh buffer to establish focus, which was stabilized using an autofocus system based on total internal reflection. Once focus was set, 1 μL of the diluted protein solution was added, and a 60-second video recorded using the Refeyn TwoMP (Refeyn, Oxford, UK). Mass-contrast calibration was performed prior to data export using a native protein marker (Thermo Fisher). Since mass photometry relies on globular proteins to generate a mass calibration curve, these markers were essential. Finally, data analysis was carried out using Refeyn DiscoverMP 2024 R2.

CRediT authorship contribution statement

María Conde-Giménez: Writing – review & editing, Writing – original draft, Methodology, Formal analysis. **Sandra Salillas:** Writing – review & editing, Methodology. **María Galiana-Cameo:** Writing – review & editing, Methodology. **Juan E. Martínez-Oliván:** Writing – review & editing, Methodology. **Alejandro Mahía:** Writing – review & editing, Methodology. **Manuel Ledesma:** Writing – review & editing, Methodology. **Juan José Galano-Frutos:** Writing – review & editing, Methodology, Formal analysis. **Ritwik Maity:** Writing – review & editing, Methodology, Formal analysis. **Adrián Velázquez-Campoy:**

Writing – review & editing, Methodology, Formal analysis. **María D. Díaz-de-Villegas:** Writing – review & editing, Resources, Methodology, Formal analysis. **Ramón Hurtado-Guerrero:** Writing – review & editing, Resources, Methodology, Formal analysis. **Javier Sancho:** Writing – review & editing, Writing – original draft, Resources, Methodology, Funding acquisition, Formal analysis, Conceptualization.

Funding

We acknowledge financial support to JS from grants PID2019–107293GB-I00 and PID2022–141068NB-I00 (MICINN, Spain); NEUROMED (Interreg-SUDOE, EU); PRECIPITA (FECYT, Spain); and E45_20R and E45_23R (Gobierno de Aragón, Spain). MC-G was recipient of a predoctoral contract from Gobierno de Aragón, Spain. This project has received funding from the European Union's Horizon 2020 research and innovation programme under grant agreement No 101004806 (MOSBRI-2024–271).

Declaration of Competing Interest

The authors have declared that no conflict of interest exists.

Acknowledgments

We thank the synchrotron radiation sources DLS (Oxford) and in particular the I24 beamline (experiment number MX14739–6). We acknowledge technical support by the SPC facility at EMBL Hamburg.

Appendix A. Supporting information

Supplementary data associated with this article can be found in the online version at doi:10.1016/j.biopha.2026.119371.

Data availability

Data will be made available on request.

References

[1] V. Orgogozo, B. Morizot, A. Martin, The differential view of genotype-phenotype relationships, Front. Genet. 6 (2015), https://doi.org/10.3389/fgene.2015.00179.

[2] M.F. Berger, E.R. Mardis, The emerging clinical relevance of genomics in cancer medicine, Nat. Rev. Clin. Oncol. 15 (2018) 353–365, https://doi.org/10.1038/s41571-018-0002-6.

[3] S. Kure, D.-C. Hou, T. Ohura, H. Iwamoto, S. Suzuki, N. Sugiyama, O. Sakamoto, K. Fujii, Y. Matsubara, K. Narisawa, Tetrahydrobiopterin-responsive phenylalanine hydroxylase deficiency, J. Pediatr. 135 (1999) 375–378, https://doi.org/10.1016/s0022-3476(99)70138-1.

[4] B. Fiege, N. Blau, Assessment of Tetrahydrobiopterin (BH4) Responsiveness in Phenylketonuria, J. Pediatr. 150 (2007) 627–630, https://doi.org/10.1016/j.jpeds.2007.02.017.

[5] F.R. Vogenberg, C. Isaacson Barash, M. Pursel, Personalized medicine: part 1: evolution and development into theranostics, Pharm. Ther. 35 (2010) 560–576.

[6] D. Grasso, S. Galderisi, A. Santucci, A. Bernini, Pharmacological chaperones and protein conformational diseases: approaches of computational structural biology, Int. J. Mol. Sci. 24 (2023) 5819, https://doi.org/10.3390/ijms24065819.

[7] M. Convertino, J. Das, N.V. Dokholyan, Pharmacological chaperones: design and development of new therapeutic strategies for the treatment of conformational diseases, ACS Chem. Biol. 11 (2016) 1471–1489, https://doi.org/10.1021/acschembio.6b00195.

[8] G. Parenti, Treating lysosomal storage diseases with pharmacological chaperones: from concept to clinics, EMBO Mol. Med. 1 (2009) 268–279, https://doi.org/10.1002/emmm.200900036.

[9] H. Li, E. Pesce, D.N. Sheppard, A.K. Singh, N. Pedemonte, Therapeutic approaches to CFTR dysfunction: from discovery to drug development, J. Cyst. Fibros. 17 (2018) S14–S21, https://doi.org/10.1016/j.jcf.2017.08.013.

[10] A. Hillert, Y. Anikster, A. Belanger-Quintana, A. Burlina, B.K. Burton, C. Carducci, A.E. Chiesa, J. Christodoulou, M. Đorđević, L.R. Desviat, A. Eliyahu, R.A.F. Evers, L. Fajkusova, F. Feillet, P.E. Bonfim-Freitas, M. Giżewska, P. Gundorova, D. Karall, K. Kneller, S.I. Kutsev, V. Leuzzi, H.L. Levy, U. Lichter-Konecki, A.C. Muntau, F. Namour, M. Oltarzewski, A. Paras, B. Perez, E. Polak, A.V. Polyakov, F. Porta, M. Rohrbach, S. Scholl-Bürgi, N. Spécola, M. Stojiljković, N. Shen, L.C. Santana-da Silva, A. Skouma, F. Van Spronsen, V. Stoppioni, B. Thöny, F.K. Trefz, J. Vockley, Y. Yu, J. Zschocke, G.F. Hoffmann, S.F. Garbade, N. Blau, The Genetic Landscape and epidemiology of phenylketonuria, Am. J. Hum. Genet. 107 (2020) 234–250, https://doi.org/10.1016/j.ajhg.2020.06.006.

[11] N. Blau, N. Shen, C. Carducci, Molecular genetics and diagnosis of phenylketonuria: state of the art, Expert Rev. Mol. Diagn. 14 (2014) 655–671, https://doi.org/10.1586/14737159.2014.923760.

[12] N. Blau, F.J. Van Spronsen, H.L. Levy, Phenylketonuria, Lancet 376 (2010) 1417–1427, https://doi.org/10.1016/s0140-6736(10)60961-0.

[13] C. Harding, New era in treatment for phenylketonuria: pharmacologic therapy with sapropterin dihydrochloride, Biol. Targ. Ther. (2010) 231, https://doi.org/10.2147/btt.s3015.

[14] K. Anjema, M. Van Rijn, F.C. Hofstede, A.M. Bosch, C.E. Hollak, E. Rubio-Gozalbo, M.C. De Vries, M.C. Janssen, C.C. Boelen, J.G. Burgerhof, N. Blau, M. Heiner-Fokkema, F.J. Van Spronsen, Tetrahydrobiopterin responsiveness in phenylketonuria: prediction with the 48-hour loading test and genotype, Orphanet J. Rare Dis. 8 (2013) 103, https://doi.org/10.1186/1750-1172-8-103.

[15] A. Gámez, L. Wang, M. Straub, M.G. Patch, R.C. Stevens, Toward PKU enzyme replacement therapy: PEGylation with activity retention for three forms of recombinant phenylalanine hydroxylase, Mol. Ther. 9 (2004) 124–129, https://doi.org/10.1016/j.ymthe.2003.11.002.

[16] N. Longo, D. Dimmock, H. Levy, K. Viau, H. Bausell, D.A. Bilder, B. Burton, C. Gross, H. Northrup, F. Rohr, S. Sacharow, A. Sanchez-Valle, M. Stuy, J. Thomas, J. Vockley, R. Zori, C.O. Harding, Evidence- and consensus-based recommendations for the use of pegvaliase in adults with phenylketonuria, Genet. Med. 21 (2019) 1851–1867, https://doi.org/10.1038/s41436-018-0403-z.

[17] J. Thomas, H. Levy, S. Amato, J. Vockley, R. Zori, D. Dimmock, C.O. Harding, D. A. Bilder, H.H. Weng, J. Olbertz, M. Merilainen, J. Jiang, K. Larimore, S. Gupta, Z. Gu, H. Northrup, Pegvaliase for the treatment of phenylketonuria: results of a long-term phase 3 clinical trial program (PRISM), Mol. Genet. Metab. 124 (2018) 27–38, https://doi.org/10.1016/j.ymgme.2018.03.006.

[18] H. Erlandsen, A.L. Pey, A. Gámez, B. Pérez, L.R. Desviat, C. Aguado, R. Koch, S. Surendran, S. Tyring, R. Matalon, C.R. Scriver, M. Ugarte, A. Martínez, R. C. Stevens, Correction of kinetic and stability defects by tetrahydrobiopterin in phenylketonuria patients with certain phenylalanine hydroxylase mutations, Proc. Natl. Acad. Sci. U. S. A. 101 (2004) 16903–16908, https://doi.org/10.1073/pnas.0407256101.

[19] A.L. Pey, B. Pérez, L.R. Desviat, M.A. Martínez, C. Aguado, H. Erlandsen, A. Gámez, R.C. Stevens, M. Thórólfsson, M. Ugarte, A. Martínez, Mechanisms underlying responsiveness to tetrahydrobiopterin in mild phenylketonuria mutations: responsiveness to Tetrahydrobiopterin IN MILD PKU, Hum. Mutat. 24 (2004) 388–399, https://doi.org/10.1002/humu.20097.

[20] A.L. Pey, M. Ying, N. Cremades, A. Velazquez-Campoy, T. Scherer, B. Thöny, J. Sancho, A. Martinez, Identification of pharmacological chaperones as potential therapeutic agents to treat phenylketonuria, J. Clin. Invest 118 (2008) 2858–2867, https://doi.org/10.1172/jci34355.

[21] R. Torreblanca, E. Lira-Navarrete, J. Sancho, R. Hurtado-Guerrero, Structural and mechanistic basis of the interaction between a pharmacological chaperone and human phenylalanine hydroxylase, ChemBioChem 13 (2012) 1266–1269, https://doi.org/10.1002/cbic.201200188.

[22] M. Conde-Giménez, J.J. Galano-Frutos, M. Galiana-Cameo, A. Mahía, B.L. Victor, S. Salillas, A. Velázquez-Campoy, R.M.M. Brito, J.A. Gálvez, M.D. Díaz-de-Villegas, J. Sancho, Alchemical design of pharmacological chaperones with higher affinity for phenylalanine hydroxylase, Int. J. Mol. Sci. 23 (2022) 4502, https://doi.org/10.3390/ijms23094502.

[23] S. Santos-Sierra, J. Kirchmair, A.M. Perna, D. Reiß, K. Kemter, W. Röschinger, H. Glossmann, S.W. Gersting, A.C. Muntau, G. Wolber, F.B. Lagler, Novel pharmacological chaperones that correct phenylketonuria in mice, Hum. Mol. Genet. 21 (2012) 1877–1887, https://doi.org/10.1093/hmg/dds001.

[24] I. Becher, T. Werner, C. Doce, E.A. Zaal, I. Tögel, C.A. Khan, A. Rueger, M. Muelbaier, E. Salzer, C.R. Berkers, P.F. Fitzpatrick, M. Bantscheff, M. M. Savitski, Thermal profiling reveals phenylalanine hydroxylase as an off-target of panobinostat, Nat. Chem. Biol. 12 (2016) 908–910, https://doi.org/10.1038/nchembio.2185.

[25] C.A. Lipinski, F. Lombardo, B.W. Dominy, P.J. Feeney, Experimental and computational approaches to estimate solubility and permeability in drug discovery and development settings 1PII of original article: S0169-409X(96)00423-1. The article was originally published in Advanced Drug Delivery Reviews 23 (1997) 3–25. 1, Adv. Drug Deliv. Rev. 46 (2001) 3–26, https://doi.org/10.1016/s0169-409x(00)00129-0.

[26] A. Daina, V. Zoete, A boiled-egg to predict gastrointestinal absorption and brain penetration of small molecules, ChemMedChem 11 (2016) 1117–1121, https://doi.org/10.1002/cmdc.201600182.

[27] P.F. Fitzpatrick, The aromatic amino acid hydroxylases: structures, catalysis, and regulation of phenylalanine hydroxylase, tyrosine hydroxylase, and tryptophan hydroxylase, Arch. Biochem. Biophys. 735 (2023) 109518, https://doi.org/10.1016/j.abb.2023.109518.

[28] M. Conde-Giménez, J. Sancho, Unravelling the complex denaturant and thermal-induced unfolding equilibria of human phenylalanine hydroxylase, Int. J. Mol. Sci. 22 (2021) 6539, https://doi.org/10.3390/ijms22126539.

[29] J. Sancho, M. Bueno, L.A. Campos, J. Fernandez-Recio, M.P. Iran, J. Lopez, C. Machicado, I. Pedroso, M. Toja, The 'relevant' stability of proteins with equilibrium intermediates, Sci. World J. 2 (2002) 1209–1215, https://doi.org/10.1100/tsw.2002.196.

[30] E. Lamazares, S. Vega, P. Ferreira, M. Medina, J.J. Galano-Frutos, M. Martínez-Júlvez, A. Velázquez-Campoy, J. Sancho, Direct examination of the relevance for folding, binding and electron transfer of a conserved protein folding intermediate,

Phys. Chem. Chem. Phys. 19 (2017) 19021–19031, https://doi.org/10.1039/C7CP02606D.

[31] E. Lamazares, I. Clemente, M. Bueno, A. Velázquez-Campoy, J. Sancho, Rational stabilization of complex proteins: a divide and combine approach, Sci. Rep. 5 (2015) 9129, https://doi.org/10.1038/srep09129.

[32] H. Erlandsen, F. Fusetti, A. Martinez, E. Hough, T. Flatmark, R.C. Stevens, Crystal structure of the catalytic domain of human phenylalanine hydroxylase reveals the structural basis for phenylketonuria, Nat. Struct. Mol. Biol. 4 (1997) 995–1000, https://doi.org/10.1038/nsb1297-995.

[33] H. Erlandsen, T. Flatmark, R.C. Stevens, E. Hough, Crystallographic analysis of the human phenylalanine hydroxylase catalytic domain with bound catechol inhibitors at 2.0 Å resolution, Biochemistry 37 (1998) 15638–15646, https://doi.org/10.1021/bi9815290.

[34] O.A. Andersen, A.J. Stokka, T. Flatmark, E. Hough, 2.0Å Resolution crystal structures of the ternary complexes of human phenylalanine hydroxylase catalytic domain with Tetrahydrobiopterin and 3-(2-Thienyl)-l-alanine or l-Norleucine: substrate specificity and molecular motions related to substrate binding, J. Mol. Biol. 333 (2003) 747–757, https://doi.org/10.1016/j.jmb.2003.09.004.

[35] K.E. Goodwill, C. Sabatier, C. Marks, R. Raag, P.F. Fitzpatrick, R.C. Stevens, Crystal structure of tyrosine hydroxylase at 2.3 Å and its implications for inherited neurodegenerative diseases, Nat. Struct. Mol. Biol. 4 (1997) 578–585, https://doi.org/10.1038/nsb0797-578.

[36] I. Müller, Guidelines for the successful generation of protein–ligand complex crystals, Acta Crystallogr D. Struct. Biol. 73 (2017) 79–92, https://doi.org/10.1107/s2059798316020271.

[37] A.M. Hassell, G. An, R.K. Bledsoe, J.M. Bynum, H.L. Carter, S.-J.J. Deng, R. T. Gampe, T.E. Grisard, K.P. Madauss, R.T. Nolte, W.J. Rocque, L. Wang, K. L. Weaver, S.P. Williams, G.B. Wisely, R. Xu, L.M. Shewchuk, Crystallization of protein–ligand complexes, Acta Crystallogr D. Biol. Crystallogr 63 (2007) 72–79, https://doi.org/10.1107/s0907444906047020.

[38] L. Ciccone, L. Vera, L. Tepshi, L. Rosalia, A. Rossello, E.A. Stura, Multicomponent mixtures for cryoprotection and ligand solubilization, Biotechnol. Rep. 7 (2015) 120–127, https://doi.org/10.1016/j.btre.2015.05.008.

[39] D. Patel, J. Kopec, F. Fitzpatrick, T.J. McCorvie, W.W. Yue, Structural basis for ligand-dependent dimerization of phenylalanine hydroxylase regulatory domain, Sci. Rep. 6 (2016), https://doi.org/10.1038/srep23748.

[40] E.C. Arturo, K. Gupta, M.R. Hansen, E. Borne, E.K. Jaffe, Biophysical characterization of full-length human phenylalanine hydroxylase provides a deeper understanding of its quaternary structure equilibrium, J. Biol. Chem. 294 (2019) 10131–10145, https://doi.org/10.1074/jbc.ra119.008294.

[41] J.-Q. Fan, A counterintuitive approach to treat enzyme deficiencies: use of enzyme inhibitors for restoring mutant enzyme activity, Biol. Chem. 389 (2008) 1–11, https://doi.org/10.1515/bc.2008.009.

[42] S. Wettstein, J. Underhaug, B. Perez, B.D. Marsden, W.W. Yue, A. Martinez, N. Blau, Linking genotypes database with locus-specific database and genotype–phenotype correlation in phenylketonuria, Eur. J. Hum. Genet. 23 (2015) 302–309, https://doi.org/10.1038/ejhg.2014.114.

[43] N.L. Steele, J.A. Plumb, L. Vidal, J. Tjørnelund, P. Knoblauch, A. Rasmussen, C. E. Ooi, P. Buhl-Jensen, R. Brown, T.R.J. Evans, J.S. DeBono, A Phase 1 pharmacokinetic and pharmacodynamic study of the histone deacetylase inhibitor belinostat in patients with advanced solid tumors, Clin. Cancer Res. 14 (2008) 804–810, https://doi.org/10.1158/1078-0432.CCR-07-1786.

[44] U.S. Food and Drug Administration, BELEODAQ (belinostat) [Package insert] o BELEODAQ (belinostat) prescribing information, U.S. Food and Drug Administration, Silver Spring, MD, 2024. ⟨www.accessdata.fda.gov⟩ (accessed March 24, 2026).

[45] J.A. Plumb, P.W. Finn, R.J. Williams, M.J. Bandara, M.R. Romero, C.J. Watkins, N. B. La Thangue, R. Brown, Pharmacodynamic response and inhibition of growth of human tumor xenografts by the novel histone deacetylase inhibitor PXD101, Mol. Cancer Ther. 2 (2003) 721–728.

[46] E. Bjørgo, P.M. Knappskog, A. Martinez, R.C. Stevens, T. Flatmark, Partial characterization and three-dimensional-structural localization of eight mutations in exon 7 of the human phenylalanine hydroxylase gene associated with phenylketonuria, Eur. J. Biochem. 257 (1998) 1–10, https://doi.org/10.1046/j.1432-1327.1998.2570001.x.

[47] E. Bjørgo, R.M.N. De Carvalho, T. Flatmark, A comparison of kinetic and regulatory properties of the tetrameric and dimeric forms of wild-type and Thr427→Pro mutant human phenylalanine hydroxylase: contribution of the flexible hinge region Asp425–Gln429 to the tetramerization and cooperative substrate binding, Eur. J. Biochem. 268 (2001) 997–1005, https://doi.org/10.1046/j.1432-1327.2001.01958.x.

[48] J. Sancho, The stability of 2-state, 3-state and more-state proteins from simple spectroscopic techniques… plus the structure of the equilibrium intermediates at the same time, Arch. Biochem. Biophys. 531 (2013) 4–13, https://doi.org/10.1016/j.abb.2012.10.014.

[49] A. Velázquez-Campoy, H. Ohtaka, A. Nezami, S. Muzammil, E. Freire, Isothermal Titration Calorimetry, CP Cell Biol. 23 (2004), https://doi.org/10.1002/0471143030.cb1708s23.

[50] W. Kabsch, XDS, Acta Crystallogr D. Biol. Crystallogr 66 (2010) 125–132, https://doi.org/10.1107/S0907444909047337.

[51] P. Evans, Scaling and assessment of data quality, Acta Crystallogr D. Biol. Crystallogr 62 (2006) 72–82, https://doi.org/10.1107/s0907444905036693.

[52] A. Vagin, A. Teplyakov, *MOLREP*: an automated program for molecular replacement, J. Appl. Crystallogr 30 (1997) 1022–1025, https://doi.org/10.1107/s0021889897006766.

[53] P. Emsley, K. Cowtan, *Coot*: model-building tools for molecular graphics, Acta Crystallogr D. Biol. Crystallogr 60 (2004) 2126–2132, https://doi.org/10.1107/s0907444904019158.

[54] G.N. Murshudov, A.A. Vagin, E.J. Dodson, Refinement of Macromolecular Structures by the Maximum-Likelihood Method, Acta Crystallogr D. Biol. Crystallogr 53 (1997) 240–255, https://doi.org/10.1107/s0907444996012255.

[55] R.A. Laskowski, M.W. MacArthur, D.S. Moss, J.M. Thornton, PROCHECK: a program to check the stereochemical quality of protein structures, J. Appl. Crystallogr 26 (1993) 283–291, https://doi.org/10.1107/s0021889892009944.

[56] O. Trott, A.J. Olson, AutoDock Vina: improving the speed and accuracy of docking with a new scoring function, efficient optimization and multithreading, J. Comput. Chem. 31 (2010) 455–461, https://doi.org/10.1002/jcc.21334.

[57] J. Eberhardt, D. Santos-Martins, A.F. Tillack, S. Forli, AutoDock Vina 1.2.0: New Docking Methods, Expanded Force Field, and Python Bindings, J. Chem. Inf. Model 61 (2021) 3891–3898, https://doi.org/10.1021/acs.jcim.1c00203.

[58] G.M. Morris, R. Huey, W. Lindstrom, M.F. Sanner, R.K. Belew, D.S. Goodsell, A. J. Olson, AutoDock4 and AutoDockTools4: automated docking with selective receptor flexibility, J. Comput. Chem. 30 (2009) 2785–2791, https://doi.org/10.1002/jcc.21256.

[59] D. Van Der Spoel, E. Lindahl, B. Hess, G. Groenhof, A.E. Mark, H.J.C. Berendsen, GROMACS: fast, flexible, and free, J. Comput. Chem. 26 (2005) 1701–1718, https://doi.org/10.1002/jcc.20291.